

# Abstract

The era of gravitational waves astronomy was ushered in by the LIGO (Laser Interferometer Gravitational-Wave Observatory) collaboration with the detection of a binary black hole collision [2]. The event that shook the foundation of space-time allowed mankind to view the cosmos in a way that had never been done previously. Since then, another remarkable event was found by the LIGO and Virgo detectors where two neutron stars collided sending both gravitational and electromagnetic waves to earth [3]. LIGO was built with the purpose of detecting the ripples in space-time caused by astrophysical events with the hopes of understanding the complexities hidden within the cosmos. In 2011, the primary stages of Advanced LIGO were installed and commissioned to start the first observing run (O1). During the writing of this thesis, the detectors had hardware replaced in order to mitigate noise from scattered light and new optics which reduced the losses from absorption. The upgrades were in preparation for the third observing run (O3) and the work presented here is primarily focused on experimental techniques for operating at higher power and mode matching Gaussian beams in the dual-recycled Michelson interferometer for the Advanced LIGO era and beyond. The first two chapters discuss the fundamentals of gravitational waves and the LIGO detector configurations. The third chapter introduces the reader to fundamentals in mode matching Gaussian laser beams. The fourth and fifth chapter summarizes the author's work at Syracuse University and LIGO Hanford observatory in mode sensing and high-powered commissioning.

# Adaptive Mode Matching in Advanced LIGO

Thomas Vo

Spring 2017

# Acknowledgements

I would like to thank my thesis advisor Stefan Ballmer for trusting in me as a scientist, always being there for indispensable advice to push forward, and letting me work on whatever I found interesting and useful.

To Peter Saulson, your stories, love of science, and intuition truly inspires me to be a better scientist and teacher.

To Duncan Brown, being asked questions at the board during group meetings always made me sweat a little but it also made me a better physicist.

To Sheila Dwyer, Jenne Driggers, and Georgia Mansell, thank you for your patience in teaching me the gritty details about the Hanford interferometer, I will never forget the difficult in-chamber work on HAM6 and the long commissioning hours in the control room.

To Daniel Sigg, the dinners were always amazing and thank you for letting me participate in some of the crucial interferometer tasks. Even when I was stuck, you were able to give crucial advice

To Keita Kawabe, thank you for the tough questions but also the encouragement to do the best science possible.

To Rick Savage, the Fellows program is one of the best parts of being at Hanford and I was honored to be a part of it for so long, thank you for the advice about all aspects of life and the fishing trips just when I needed it most.

To Aidan Brooks, thank you for letting me work on/use TCS at Hanford, your guidance and experience is invaluable in times of confusion.

To Daniel Vander-Hyde, thank you for helping at Hanford with your extra hands/brain and being patient with me when things weren't going well but also celebrating with me when things were!

To Dan Brown, thanks for coming across the pond to help when we needed it most and the Inbetweeners jokes at wings night.

To Corey Gray, Gunner and Gomez, the hikes brought peace to my troubled mind and patience to my un-restful soul.

To all the operators and staff at Hanford: Jeff, Betsy, Chandra, TJ, Jim, Cheryl, Nico, Patrick, Ed, Gerardo, Evan.

To Hang Yu: Thank you for helping me understand the inner workings of the interferometer with only a few lines of math and a picture.

To my forever teachers Melissa Brainerd, Paul Didier, Chrissy Dahms, Carolyn West, and Dan Dorsey: The accumulated effect of my work is a direct result of your teachings, you inspire kids like me from White Center to chase our dreams.

To my childhood friends Quang, Leah, Thang, Sienna, Khanh, Truc, Kay, Tuan, Wanda, James, Matt and Trung: You knew me when I was just dreaming of being a scientist, now we're here.

To the Bloomingdale family: Thank you for always making me feel at home even in the coldest of Syracuse winters.

To Jaysin Lord, Laura Nuttall, and Mat Hutchens: Thank you for the laughs and Thursday wings.

To my family Cuong, Nhi, Tony, Theresa, Brittney, Kayla, Chloe: Your support and encouragement mean everything to me.

To my parents: The difficulties of science dwindle in comparison to your journey from Vietnam, this work is dedicated to you.

To my darling Tiffany: Your support provides nourishment for my soul and your love gives a guiding light through the darkest of nights.

# Contents

Preface	3
<b>1 Wavefront Control at LIGO Hanford</b>	<b>5</b>
1.1 Hot vs. Cold Interferometers . . . . .	6
1.1.1 Thermal Lensing . . . . .	6
1.2 Wavefront Distortions from Thermal Effects . . . . .	9
1.3 Contrast Defect . . . . .	15
1.3.1 Simple Michelson Contrast Defect . . . . .	16
1.3.2 Modal Contrast Defect . . . . .	17
1.4 Tuning Thermal Compensation for LIGO . . . . .	18
1.4.1 Hartmann Wavefront Sensors . . . . .	19
1.4.2 Ring Heater and CO <sub>2</sub> Commissioning . . . . .	28
1.5 Point Absorbers . . . . .	33
1.6 Higher Power Operation . . . . .	36
1.7 Mode Matching from the OPO to the OMC . . . . .	43

# Chapter 1

## Wavefront Control at LIGO Hanford

Simulations and calculations are wonderful guides to understanding and building intuition about mode matching, however, no model is perfect and experiments have a way of presenting the most interesting and challenging problems. Preparation for the third observing run (O3) required extensive work to understand Advanced LIGO’s path to achieve higher arm power. One of the most important tasks was tuning the thermal compensation and interferometer sensing/controls systems in order to maintain the power build-ups in the PRC and arms during nominal low noise operation. This chapter will build some constructs on how lensing affects the interferometer fields and a few strategies to tune the Thermal Compensation System (TCS) at LIGO Hanford. Then summarizing a few in-situ measurements taken to understand the mode content at the output mode cleaner in single bounce configuration

For Advanced LIGO, optic heating comes from two sources: one main source is absorption by arm cavity optics from the main interferometer beam and another source is the effects of TCS which are meant to combat the wavefront distortion by applying heat in key places. Thermal compensation currently utilizes ring heaters at all four main test masses, a disk heater at the SR3, and CO<sub>2</sub> lasers at the input test masses.

## 1.1 Hot vs. Cold Interferometers

When fully operational, the arm cavities can have approximately 150 kilowatts of circulating power. An estimated but useful description of the total arm power in each arm is

$$P_{\text{ARM}} \approx \frac{1}{2}(g_{\text{PRC}} * g_{\text{ARM}} * P_{\text{in}}) \quad (1.1)$$

where  $g_{\text{PRC}} \approx 45$  is the power recycling cavity gain and  $g_{\text{ARM}} \approx 225$  is the single arm cavity gain. For O3, the intended input power  $P_{\text{in}}$  will reach approximately 30 W which means  $P_{\text{ARM}} \approx 150,000$  W. A fraction of that power between 0.2-0.8 PPM, will be absorbed by the high reflectivity surface creating a *thermo-elastic* effect which changes the radius of curvature. By changing the test mass curvatures, the resonant Gaussian mode will also change its profile. Additionally, the *thermo-refractive* effect will vary the index of refraction within the bulk as a function of absorbed temperature which creates a thermal lens that turns out to be an order of magnitude larger than the wavefront distortion from therm-elastic effects in fused silica [89].

### 1.1.1 Thermal Lensing

As seen in Section ??, the sideband and carrier frequencies propagate differently in the interferometer by design, which means their fields see different thermal lensing effects. The ITM substrate which sees the thermo-refractive change from absorption will play the largest role because the carrier is not affected to first order, this will be shown in Section 1.1.1. To understand how the fields change, the easiest way is to invoke the ABCD transfer matrix approach to track how the phase changes as they propagate through the optical system [60].

#### Carrier

The carrier is resonant in the 4 kilometer arm cavities as well as the PRC, so a simplified model resembles a coupled cavity setup where there is already a locked resonator with some

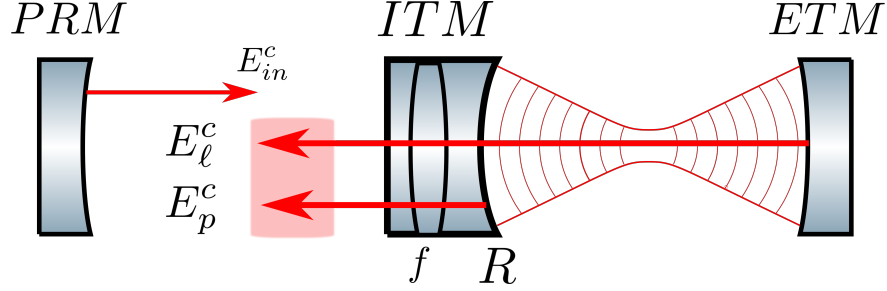


**Figure 1.1: A simplified model for the effect of a substrate thermal lens on the carrier field.** An input beam,  $E_{\text{in}}^c$ , from the power recycling mirror (PRM) will have a radius of curvature that mode matches to the input test mass (ITM). The promptly reflected beam,  $E_p^c$ , is denoted by equation 1.4 and the leakage beam,  $E_\ell^c$ , is expressed by equation 1.5 where the sum of them would make the total reflected beam. The leakage field will have the same shape as the ITM radius of curvature  $R$  when exiting the arm and see the thermal lensing  $f$ . The promptly reflected field will also see the lens  $f$  twice but when combined with the leakage beam, the *total* reflected field is not affected by the thermal lens.

leakage beam and there is an input mode propagating from the power recycling cavity. Consider the diagram in Figure 1.1, a two-mirror optical system which has an input carrier beam,  $|E_{\text{in}}^c\rangle$ , that has a portion promptly reflected off the input mirror to create  $|E_p^c\rangle$

$$|E_p^c\rangle = \hat{M}_p^c |E_{\text{in}}^c\rangle \quad (1.2)$$

The prompt reflection is made up of a beam incident on a converging lens(-) from the substrate and a single reflection from the input coupler's convex(+) surface, therefore, the transfer matrix is

$$\hat{M}_p^c = \begin{bmatrix} 1 & 0 \\ -\frac{1}{f} & 1 \end{bmatrix} \begin{bmatrix} 1 & 0 \\ +\frac{2}{R} & 1 \end{bmatrix} \begin{bmatrix} 1 & 0 \\ -\frac{1}{f} & 1 \end{bmatrix} \quad (1.3)$$

where  $R$  is the radius of curvature of the high reflectivity surface and  $f$  is the focal length of the mirror substrate. In general, this can be a combination of the static lens and any thermal effects which create additional (intentional or non-intentional) lensing.

$$|E_p^c\rangle = \hat{M}_p^c \begin{bmatrix} 1 \\ \frac{1}{q_{in}} \end{bmatrix} = \begin{bmatrix} 1 \\ \frac{1}{q_{in}} + 2\left(\frac{1}{R} - \frac{1}{f}\right) \end{bmatrix} = \begin{bmatrix} 1 \\ \frac{1}{q_p} \end{bmatrix} \quad (1.4)$$

In addition, there is also a circulating field inside the cavity which leaks out can be denoted by  $|E_\ell^c\rangle$  which exits with the input coupler's radius of curvature and sees a single pass through the substrate lens,

$$|E_\ell^c\rangle = \begin{bmatrix} 1 & 0 \\ -\frac{1}{f} & 1 \end{bmatrix} \begin{bmatrix} 1 \\ \frac{1}{R} \end{bmatrix} = \begin{bmatrix} 1 \\ \frac{1}{R} - \frac{1}{f} \end{bmatrix} \quad (1.5)$$

The total reflected beam is a summation of the prompt and leaked cavity fields. LIGO uses arms which are highly over-coupled optical cavities so the promptly reflected amplitude is  $|E_p^c| \approx |E_{in}|$  and using equation ??, the leakage amplitude is  $|E_\ell^c| \approx -2|E_{in}|$ . Putting all this together, the total reflected field of the carrier is

$$\begin{aligned} E_{REFL}^c &= E_\ell^c + E_p^c \\ &= E_{in} \left[ \exp\left(\frac{-ikr^2}{2q_p}\right) - 2\exp\left(\frac{-ikr^2}{2q_\ell}\right) \right] \\ &\approx E_{in} \left[ -1 - \frac{ikr^2}{2} \left( \frac{1}{q_p} - \frac{2}{q_\ell} \right) \right] \\ &\approx -E_{in} \exp\left(\frac{ikr^2}{2q_{in}}\right) \end{aligned} \quad (1.6)$$

This shows that the total reflected carrier field will be the original amplitude with a negative sign and the same absolute curvature, however, now the beam is diverging instead of converging. **The amazing part is that the end result is independent of the substrate lensing to first order.** The point where this model breaks down is when the power recycling mode is altered so much by the lens that it is no longer well matched to the arms such that the input beam does not have the right radius of curvature. At this point, there will be extra losses from higher order mode-coupling. Also, if the lensing becomes so bad that the radius of curvature shifts the PRC g-factors such that the resonant mode is no longer

geometrically stable (see Appendix ??), however, this requires significant thermal lensing well beyond what is expected in Advanced LIGO [60]. A numerical FINESSE model uses this simplified geometry to calculate the power recycling gain and arm build up in Figure 1.16 as a function of round trip losses and thermal lensing.

### **Sidebands**

Using the same formalism as the carrier fields, the sidebands will have the same input curvature, however, they do not resonate in the arms so there is no cavity leakage field. Therefore, the sidebands will see the phase change due to the substrate lens and this has very important consequences on the sideband build up within the power recycling cavity.

### **GW Signal**

As mentioned in Section ??, LIGO currently employs a DC readout scheme that extracts the signal by beating the carrier field with the audio frequency sidebands created by the gravitational wave. Although the carrier field was shown to be immune from substrate thermal lensing, the gravitational wave sideband field will see a single-passed lensing effect as it propagates out of the cavity and towards the beamsplitter. If there is differential lensing, the signal recycling cavity will see an effective thermal lens,  $TL_-$ , which will be scattered into higher order modes. This reduces the amount of gravitational wave signal at the anti-symmetric port that is directly proportional to the mode mismatch between the arms.

## **1.2 Wavefront Distortions from Thermal Effects**

In the previous section, it was shown that lensing in the substrate affects fields in the interferometer differently. The thermal distortions were modeled as a simple addition of phase, however, it is useful to understand how the optical path varies from first principles. This

provides theoretical groundwork for modeling interferometer heating as well as corrective measures using TCS. A lot of work in this field was introduced in the context of gravitational wave detectors by Hello and Vinet [52] [85] where they implemented the Heat Diffusion equation in order to analytically derive the phase change due to thermal aberrations. In general, there are two effects which occur when a beam interacts with an optic which has a temperature field: thermo-refractive and thermo-elastic.

The first arises from the index of refraction changing as a function of the temperature distribution  $T(r, z)$ ,

$$\Delta n_r(r, z) = \frac{dn}{dT} T(r, z) \quad (1.7)$$

where  $\frac{dn}{dT}$  is the temperature index coefficient and is dependent on the optic material. For example, if the heating source comes from a laser beam which imparts onto the optic a Gaussian-like intensity pattern, the temperature profile will be non-uniform and lead to a varying index of refraction that causes wavefront distortions (see Figure 1.2).

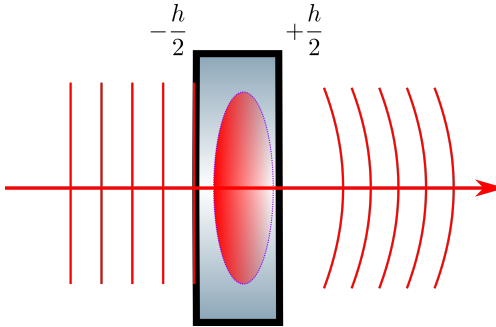


**Figure 1.2: A plane wave passing through a lens with a temperature gradient.** The index of refraction,  $n$ , depends on the material and temperature so when a plane wave moves through a medium with a non-uniform temperature field, a phase lag or lead occurs in the wavefront. Since  $\frac{dn}{dT}$  is negative, the distortion will resemble a diverging lens.

To understand how changing the index of refraction varies the optical path length, consider the function  $S(r)$  which describes surfaces that are perpendicular to the rays. If  $S(r)$  is a known function then the rays can be reconstructed using the gradient,  $\nabla S(r)$ . As an analogy to electrostatics,  $S(r)$  is similar to the potential function  $V$  and the electric field is

described by  $E = -\nabla V$ . As an extension of ray optics, Fermat's principle requires that the Eikonal equation be satisfied,

$$|\nabla S|^2 = n^2 \quad (1.8)$$

By integrating along the axis of propagation ( $\hat{z}$ ) in Figure 1.2 through the substrate, one can find the optical path distortion

$$Z(r) = \frac{dn}{dT} \int_{-h/2}^{+h/2} T(r, z) dz \quad (1.9)$$

It is clear that the temperature field is key to understanding exactly how the wavefront is distorted. In order to analytically solve for  $T(r, z)$ , one must invoke the famous Heat equation,

$$\kappa \nabla^2 T(r, z) = \rho C \frac{\partial T}{\partial t} \quad (1.10)$$

where  $\kappa$  is the thermal conductivity,  $\rho$  is the density, and  $C$  is the specific heat. A complete solution for such an equation will be a sum of two parts:

$$T(r, z, t) = T_s(r, z) + T_t(r, z, t) \quad (1.11)$$

where the first term is the steady-state solution which includes the an ambient temperature and a perturbation,  $T_s(r, z) = T_p(r, z) + T_0$ . The main goal for the remainder of the section will be finding a solution to the perturbation field. The second term is the transient time-dependent solution which will converge to the steady-state as time goes to infinity. For the LIGO test masses which are approximately cylindrical, the heat equation in steady-state equilibrium is

$$\kappa \left[ \frac{1}{r} \frac{\partial}{\partial r} \left( r \frac{\partial}{\partial r} \right) + \frac{\partial^2}{\partial z^2} \right] T_s(r, z) = 0 \quad (1.12)$$

The next step is to understand the boundary conditions using Figure 1.3 and the balance of

heat fluxes at each of the surfaces,

$$\mathbf{n} \cdot [\mathbf{F} + \kappa \nabla T_s]_{\text{surf}} = 0 \quad (1.13)$$

Assuming that the outward flux is from radiation which follows the Stefan-Boltzmann law,

$$\begin{aligned} \mathbf{n} \cdot \mathbf{F}_{t_{\text{surf}}} &= \sigma_B [T_s^4 - T_0^4] = \sigma_B [(T_p(r, z) + T_0)^4 - T_0^4] \\ &\approx 4\sigma_B T_0^3 T_p(r, z) \end{aligned} \quad (1.14)$$

where  $\sigma_B$  is the Stefan-Boltzmann's constant. It is important to note that  $\sigma_B$  depends on the material and may vary by a scalar amount but for brevity, it is used as a constant here. The last part of the equation assumes that the temperature field is only a small perturbation from the ambient surroundings,  $T_p(r, z) \ll T_0$ , which allows the radiation term to become linear. Figure 1.3 shows boundary conditions for the LIGO test masses,

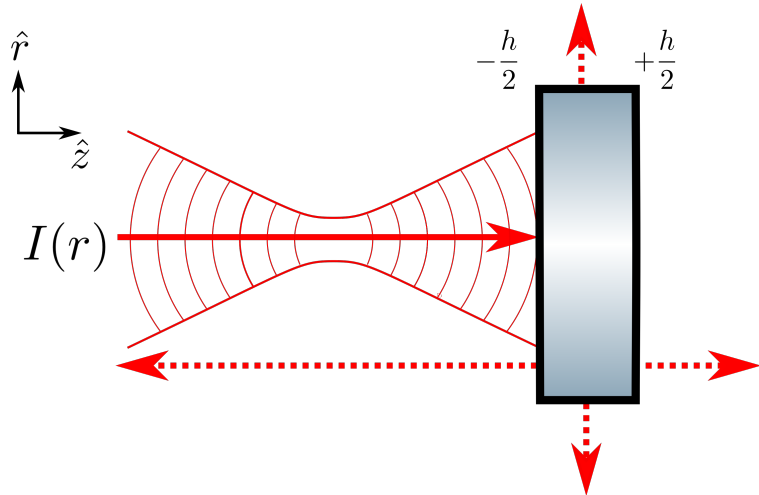


Figure 1.3: **A conceptual model of flux balance for a cylindrical object.** The red dotted lines represent the radiative fluxes escaping the optic while a Gaussian beam with intensity profile  $I(r)$  is pumping energy in as denoted by the red solid line.

At the surface where  $z = h/2$  the total flux is radiative,

$$-\kappa \frac{\partial T_p(r, h/2)}{\partial z} = 4\sigma_B T_0^3 T_p(r, h/2) \quad (1.15)$$

At the barrel of the cylinder where  $r = a$ , total flux is also radiative,

$$-\kappa \frac{\partial T_p(a, z)}{\partial r} = 4\sigma_B T_0^3 T_p(a, z) \quad (1.16)$$

At the surface where  $z = -h/2$  there are two components of flux, one is radiative and the second is the input power from the laser beam striking the optic surface,

$$-\kappa \frac{\partial T_p(r, -h/2)}{\partial z} = -4\sigma_B T_0^3 T_p(r, -h/2) + \epsilon_a I(r) \quad (1.17)$$

where  $I(r) = \frac{2P}{\pi w^2} \exp\{-2r^2/w^2\}$  is the laser beam intensity with power  $P$  over a beam size of  $w$  and  $\epsilon_a$  is the absorption coefficient. Here, the radiative term has a negative sign to represent the flux direction. Once boundary conditions are established, most introductory textbooks that deal with partial differential equations will apply an educated guess for the solution. In this case, the resulting temperature field will be a harmonic function,

$$T_p(r, \phi, z) = (Ae^{+kz} + Be^{-kz}) J_0(kr) \quad (1.18)$$

where  $J_0$  is the spherical Bessel function of the first kind and  $k$  is a constant. Although this particular temperature distribution can be even more general by allowing all the orders of  $J_n$ , this form is sufficient. Using the boundary condition from 1.16 and the property  $\frac{\partial J_0(x)}{\partial x} = -J_1(x)$ ,

$$-\kappa k \frac{\partial J_0(kr)}{\partial r} \Big|_{r=a} = 4\sigma_B T_0^3 J_0(ka) \quad (1.19)$$

$$ka J_1(ka) - \chi J_0(ka) = 0 \quad (1.20)$$

where  $\chi = 4\sigma T_0^3 a / \kappa$  is the reduced time constant. There exists an infinite number of discrete solutions which can solve 1.20 using various values of  $k_n a = \rho_n$ . The temperature field then becomes,

$$T_p(r, z) = \sum_{n=0}^{\infty} (A_n e^{+k_n z} + B_n e^{-k_n z}) J_0(k_n r) \quad (1.21)$$

In order to solve the conditions from equations 1.15 and 1.17, the strategy is to use the orthogonality of the spherical Bessel functions in order to expand the equations into a solvable algebraic form. This will include expanding the intensity profile  $I(r)$  in this basis as well. Consider the boundary from  $r = 0$  to  $r = a$ , the functions  $J_0(k_n r)$  form a complete basis set and the normalization constant is given by the Sturm-Louisville problem,

$$\int_0^a J_0(k_n r) J_0(k_m r) r dr = \delta_{mn} \frac{[\chi^2 + (k_n a)^2]}{2k_n^2} J_0^2(k_n a) = \delta_{mn} \frac{1}{N_n} \quad (1.22)$$

Then expanding the intensity profile in terms of the Bessel function:  $I(r) = \sum_n^\infty p_n J_0(k_n r)$  and inverting to solve for  $p_n$  leads to,

$$\begin{aligned} p_n &= N_n \int_0^a I(r) J_0(k_n a) r dr \\ &= N_n \int_0^a \left[ \frac{2P}{\pi w^2} \right] J_0(k_n a) \exp\{-2r^2/w^2\} r dr \\ &\approx N_n \frac{P}{2\pi a^2} \exp\left\{-\frac{(k_n w)^2}{8}\right\} \end{aligned} \quad (1.23)$$

The approximation came from integrating to infinity instead of  $a$  which is reasonable if diffraction losses are small on the substrate. Plugging in the equation 1.21 and  $I(r)$  into the remaining boundary conditions,

$$\left[ k_n - \frac{4\sigma_B T_0^3}{\kappa} \right] e^{-k_n h} A_n - \left[ k_n + \frac{4\sigma_B T_0^3}{\kappa} \right] B_n = \frac{\epsilon p_n}{\kappa} e^{-k_n h/2} \quad (1.24a)$$

$$\left[ k_n + \frac{4\sigma_B T_0^3}{\kappa} \right] A_n - \left[ k_n - \frac{4\sigma_B T_0^3}{\kappa} \right] B_n e^{-k_n h} = 0 \quad (1.24b)$$

Solving for  $A_n$  and  $B_n$ ,

$$A_n = \frac{\epsilon_a p_n}{\kappa} e^{-3k_n h/2} \frac{\eta_+}{\eta_+ - \eta_- e^{-2k_n h}} \quad (1.25a)$$

$$B_n = \frac{\epsilon_a p_n}{\kappa} e^{-k_n h/2} \frac{\eta_-}{\eta_+ - \eta_- e^{-2k_n h}} \quad (1.25b)$$

where  $\eta_\pm = k_n \pm \frac{4\sigma_B T_0^3}{\kappa}$  is used for brevity. Now it is possible to write down the entire

steady-state temperature field for a cylindrical test mass with a laser beam impinging on the surface,

$$T_p(r, z) = \sum_{n=0}^{\infty} \frac{\epsilon_a p_n}{\kappa} \frac{\eta_- e^{-k_n(3h/2-z)} + \eta_+ e^{-k_n(h/2-z)}}{\eta_+ - \eta_- e^{-2k_n h}} J_0(k_n r) \quad (1.26)$$

Once the temperature profile is solved, the path length distortion from the thermo-refractive effect can be found by solving by equation 1.9,

$$Z_{\text{TR}}(r) = \frac{dn}{dt} \frac{\epsilon_a}{\kappa} \sum_{n=0}^{\infty} \frac{p_n}{k_n} \frac{1 - e^{-k_n h}}{[\eta_+ - \eta_- e^{-k_n h}]} J_0(k_n r) \quad (1.27)$$

where  $p_n$  contains information about the heating profile so it is possible to directly plug in equation 1.23 to represent the distortion from a Gaussian beam,

$$Z_{\text{TR}}^G(r) = \frac{dn}{dt} \frac{\epsilon_a P}{2\pi a^2 \kappa} \sum_{n=0}^{\infty} \frac{N_n}{k_n} e^{-(k_n w)^2/8} \frac{1 - e^{-k_n h}}{[\eta_+ - \eta_- e^{-k_n h}]} J_0(k_n r) \quad (1.28)$$

The thermo-refractive effect due to coating and substrate absorption is only one type, there is also an effect which elastically curves the surface from thermal expansion [85]. This thermo-elastic effect deals with the internal stresses of the material and employs the stress-strain relations in order to derive the wavefront curvature. For the LIGO test masses which use fused silica, this effect is smaller than the thermo-refractive wavefront distortion by about an order of magnitude.

### 1.3 Contrast Defect

Generally, the contrast defect is defined as the ratio of power between the antisymmetric port and the reflected port when locked on a dark fringe. In other words, it is the amount of junk light that is present in the interferometer when light between the two arms do not perfectly interfere with each other. This junk light can be the symptom of various causes, for example, an imbalance of reflectivity between ITMX and ITMY will cause non-perfect destructive interference at the antisymmetric port and a camera would see a TEM00 beam

when locked on length. Another cause of contrast defect could be from misalignment between the ITMs or beamsplitter which will result in seeing a TEM 01/10 mode. However, if both of the aforementioned causes are fixed with a combination of stringent design specifications for the reflectivity and alignment loops closed to minimize angular jitter, then the contrast defect will be dominated by mode mismatch which can be fixed by a combination of ring heaters and CO<sub>2</sub> lasers. The picture gets even more complicated when adding in the absorption for individual optics and introducing multiple Fabry-Perot cavities which will treat the sidebands and carrier fields differently. One of the main goals for the Thermal Compensation System is to correct the cold and hot interferometer differences in radii of curvature.

### 1.3.1 Simple Michelson Contrast Defect

The simple Michelson can give a first estimate of the contrast defect when starting to commission the interferometer's thermal system, however, it is not used in nominal low noise since the dual-recycled Michelson is implemented. By propagating the input mode cleaner beam to the beamsplitter and taking a single bounce at the high reflectivity surface, one can approximate the resultant mode overlap by measuring the power at the antisymmetric port. The static mismatch correction was measured this way and is compensated using one of the CO<sub>2</sub> lasers to reduce the contrast at 2 Watts of input power from 0.4% to 0.1% [? ].

At this point the carrier and sideband fields follow the same ABCD matrix transfer function, so only one calculation is needed to estimate the contrast defect. A keen reader will notice that this model will not take the Schnupp asymmetry into account which allows the  $\hat{x}$ -direction beam to travel an extra 8 centimeters further than the  $\hat{y}$ , however, this effect will only change the end result by approximately 10%. In fact, for this interferometer configuration, the dominate source of mismatch will be from the prompt reflection off the HR surfaces of the ITMs where most of the phase change occurs. The sideband contribution at the antisymmetric port can be estimated by using equation ?? and measuring the modulation

depth,  $\Gamma_\Omega$ , for the 9 and 45 MHz RF fields that enter the interferometer,

$$\begin{aligned} P_{\text{SB}} &= 2P_{\text{in}} \left( \frac{\Gamma}{2} \right)^2 t_{\text{SB}\pm} \\ &= 2P_{\text{in}} \left( \frac{\Gamma}{2} \right)^2 \sin^2(k_\Omega \Delta\ell) \end{aligned} \quad (1.29)$$

Additionally, the beamsplitter RMS motion will also contribute extra power at the AS and can be estimated by calculating the coupling coefficient from the 00 to 01 HG mode,

$$P_{01} = 2P_{\text{in}} \left( \frac{\pi \alpha w(z)}{\lambda} \right)^2 \quad (1.30)$$

where  $w(z)$  is the beam size on the test mass and  $\alpha$  is the misalignment RMS.

### 1.3.2 Modal Contrast Defect

During full lock, the formalism must be extended to include the mode shape of two arm cavities interfering at the beamsplitter. Using the Laguerre-Gauss modes is useful for brevity because the mode mismatch couples to only one higher order mode. Contrast defect can be defined using the zeroth eigenmode of each arm and then expanded to project the X-arm's basis onto Y-arm using higher order LG modes,  $LG_y^{00} \rightarrow LG_x^{00} + \alpha LG_x^{10}$ . Where  $\alpha = \frac{1}{\sqrt{2}} \left( \frac{\Delta\omega_0}{\omega_0} + i \frac{\Delta z}{z_R} \right)$  is the amount of higher order mode coupling due to mismatch in beam size and location, respectively (see Chapter 3).

$$\begin{aligned} \text{CD} &\equiv \frac{P_{\text{AS}}}{P_{\text{REFL}}} \\ &= \frac{|LG_x^{00} - LG_y^{00}|^2}{|LG_x^{00} + LG_y^{00}|^2} \\ &= \frac{|LG_x^{00}|^2 + |LG_x^{00} + \alpha LG_x^{10}|^2 - 2 \text{Re}(LG_x^{00}[LG_x^{00*} + \alpha LG_x^{10}])}{|LG_x^{00}|^2 + |LG_x^{00} + \alpha LG_x^{10}|^2 + 2 \text{Re}(LG_x^{00}[LG_x^{00*} + \alpha LG_x^{10}])} \\ &\approx \frac{\alpha^2}{4} \\ &\approx \frac{1}{8} \left[ \left( \frac{\Delta\omega_0}{\omega_0} \right)^2 + \left( \frac{\Delta z}{z_R} \right)^2 \right] \end{aligned} \quad (1.31)$$

Mismatch between the arm cavities can stem from a few sources such as the difference between the radii of curvature on the high reflectivity surfaces that will cause the resonant modes to be shaped differently between the X-arm and Y-arm. LIGO tries to optimize this effect by pairing the optics based on their properties, however, during the upgrades from O2 to O3 at Hanford, ITMX was replaced but ITMY was not which lead to a static mismatch between the input test masses.

## 1.4 Tuning Thermal Compensation for LIGO

Goals: A path to higher power with preloading [89] [83]

As mentioned in Section 1.1.1, the circulating power in each of the arms can be close to 150 kW for O3 and higher for the next observation runs. Even with absorption estimates between 0.2 – 0.8 parts per million, the induced substrate lensing can be significant. The Thermal Compensation System (TCS) [60] [17] was developed to correct the wavefront by applying heat to cancel the deformities caused by interferometer heating. Lock acquisition and gravitational-wave optimization are the main metrics for success when commissioning most LIGO systems. To aid in the former, TCS is required to thermally lens the substrate between the beamsplitter and high-reflectivity surfaces of the test masses such that the optical path difference is optimized for the carrier and sideband power recycling gains. Both deal heavily with mode-matching the arm cavities such that overlap between the Gaussian modes is maximized.

To optimize the TCS settings for the best power build-ups, there are two separate strategies: The first requires estimating the amount of absorption on the test masses with the Hartmann Wavefront Sensors to measure the optical path distortion induced by the interferometer during a lock loss. Then pre-load the ring heaters with the nominal settings which would cancel carrier beam's thermal absorption in the "hot" state. The ring heaters have a very long time constant (30 hours) to reach thermal equilibrium with a step response of

electrical power, so if there is compensation needed, the heaters must be energized at all times. However, turning them on will change the radius of curvature and induce a substrate lens (see Section 1.4.2) that has to be canceled out by the CO<sub>2</sub> (Carbon Dioxide) lasers which create a lens on the compensation plate of the quadruple pendulum. Since the CO<sub>2</sub> lasers have a time constant of approximately 0.5 hours, they can be turned up during lock acquisition and reduced as needed when the interferometer input power is increased. The second method is to use relevant interferometer RF signals at various ports to experimentally adjust the lensing commonly or differentially to maintain power recycling build-ups while increasing the interferometer input power. In principle, either method should lead to the same answer but in practice, both are used to find the nominal thermal compensation configuration.

### 1.4.1 Hartmann Wavefront Sensors

All estimates of steady-state curvature changes due to heating by the main interferometer beam depend linearly on the absorption and this can be quite difficult to detect when the coating absorption are typically less than one part in a million.

In order to diagnose this effect, the Hartmann Wavefront Sensors (HWS) [13] [84] was a system developed by Adelaide and Caltech [15] [16] which use an auxiliary beams and charged-coupled imaging devices (CCD) to sense the wavefront distortions formed by heating from the interferometer beam during power up and a lock loss. Currently, there are four Hartmann sensors installed at each test mass, which are injected from the AR surface side of the optics. Technical constraints require the ITM HWSs optical paths to differ from the ETM HWSs but the concept is still the same, so for brevity, only the ITMs HWSs will be discussed in detail. In Figure 1.4, the system starts with an auxiliary super-luminous LED (SLED) beam being injected into the vacuum system and a telescope (Lens 1, Lens 2) which collimates/expands the beam to sample a space 200 mm in diameter on the test mass HR surface. The return beams are picked-off and sent to a CCD with a Hartmann

plate mounted on the front which effectively decompose the wavefront into individual rays. Using a wavefront from a previous time with a cold optic as a reference. The Hartmann code creates a gradient vector field between the two times which have information about thermal lensing, then numerically integrates the gradients to fit a wavefront distortion field. The algorithm then uses the Zernike polynomials as a single basis to represent the effect of the thermal lens. [14]

### Tuning the Hartmann Sensors

A source of systematic noise was from beam clipping in chamber on the ITMX HWS, see Figure 1.7. This creates fringes which are extremely sensitive to misalignment; one bandage that was applied to reduce this noise was to digitally mask the fringes so they do not confuse the fitting algorithms. Hand tuning must be done so the mask is wide enough and centered around the interferometer lensing but not so large that the Hartmann fitting is corrupted by the fringes. The aperture is very tight from baffles and are relatively far field from the CCD plane. Two in-air periscope mirrors with pico-motors were used for alignment but beam clipping could not be fully removed. This artifact was also found at LLO so it suggests a systematic error in the alignment scheme. A possible fix could be implemented by replacing an in-vacuum steering mirror with a pico-motor.

It was also found that the CCDs (Dalsa pantera 1m60) had a number of pixels which would create large spikes in their intensity counts and produce large artifacts in the gradient plots that corrupted the spherical lens fitting (see Figure 1.6). One of the requirements for the HWSs is a wavefront distortion resolution of 1.35 nm [17] and a single glitch could register a few orders of magnitude higher. A solution for this was implemented by using the dark images to locate the bad pixels by averaging the counts over a few minutes and finding all the pixels which have counts higher than a particular threshold, generally 1.5 times above the average ambient dark noise level (about 50 counts). The dark frames would be read in by the Hartmann code which has a module written by Adelaide that uses the dark images as

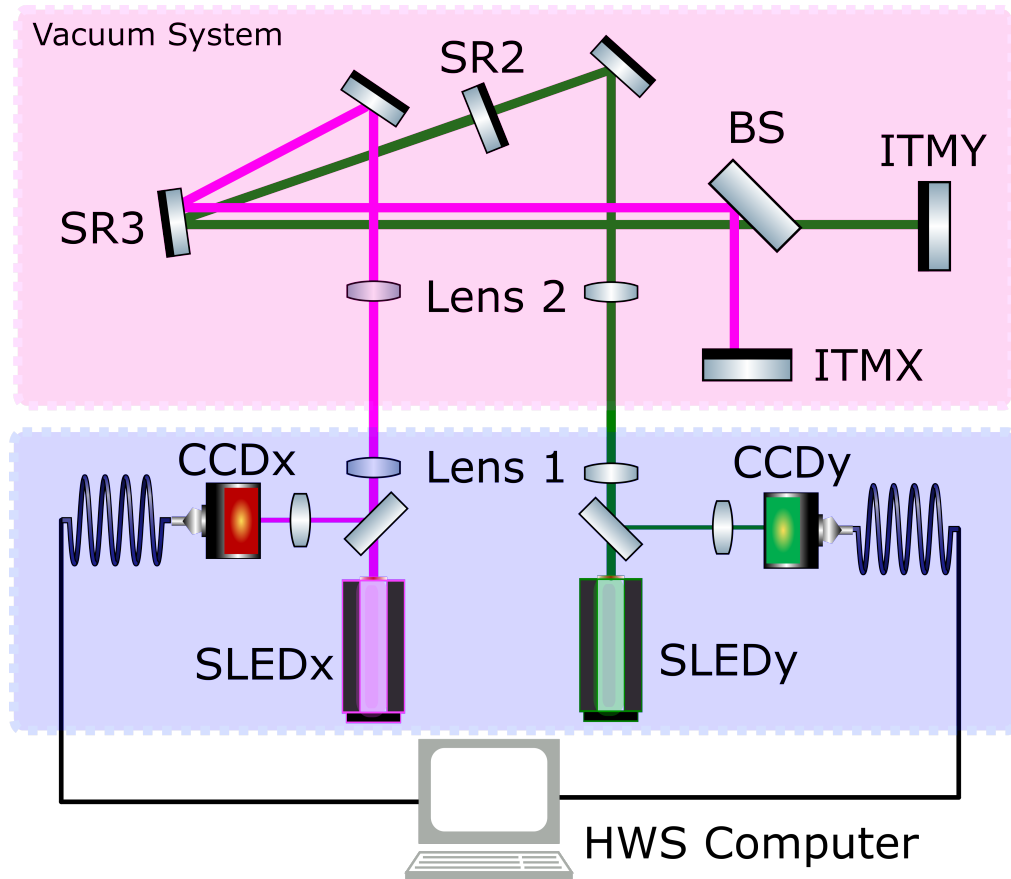


Figure 1.4: **ITM Hartmann sensors optical layout.** The path for injection is different for the two Hartmann sensors which use separate wavelengths to take advantage of the main beam splitter AR/HR surface reflectivity. The ITMX (magenta) and ITMY (green) probe beam wavelengths are 800 nm and 833 nm, respectively, and have a 40 nm linewidth [17]. The beams are sent into the vacuum system and retro-reflected off their respective optics back towards the pick-off mirrors before going into the CCDs with a Hartmann plate attached. The cameras are then sent via fiber to a computer that runs the analysis pipeline on the images and exports the data to EPICS so the users can interface with the real time digital system in the control rooms.

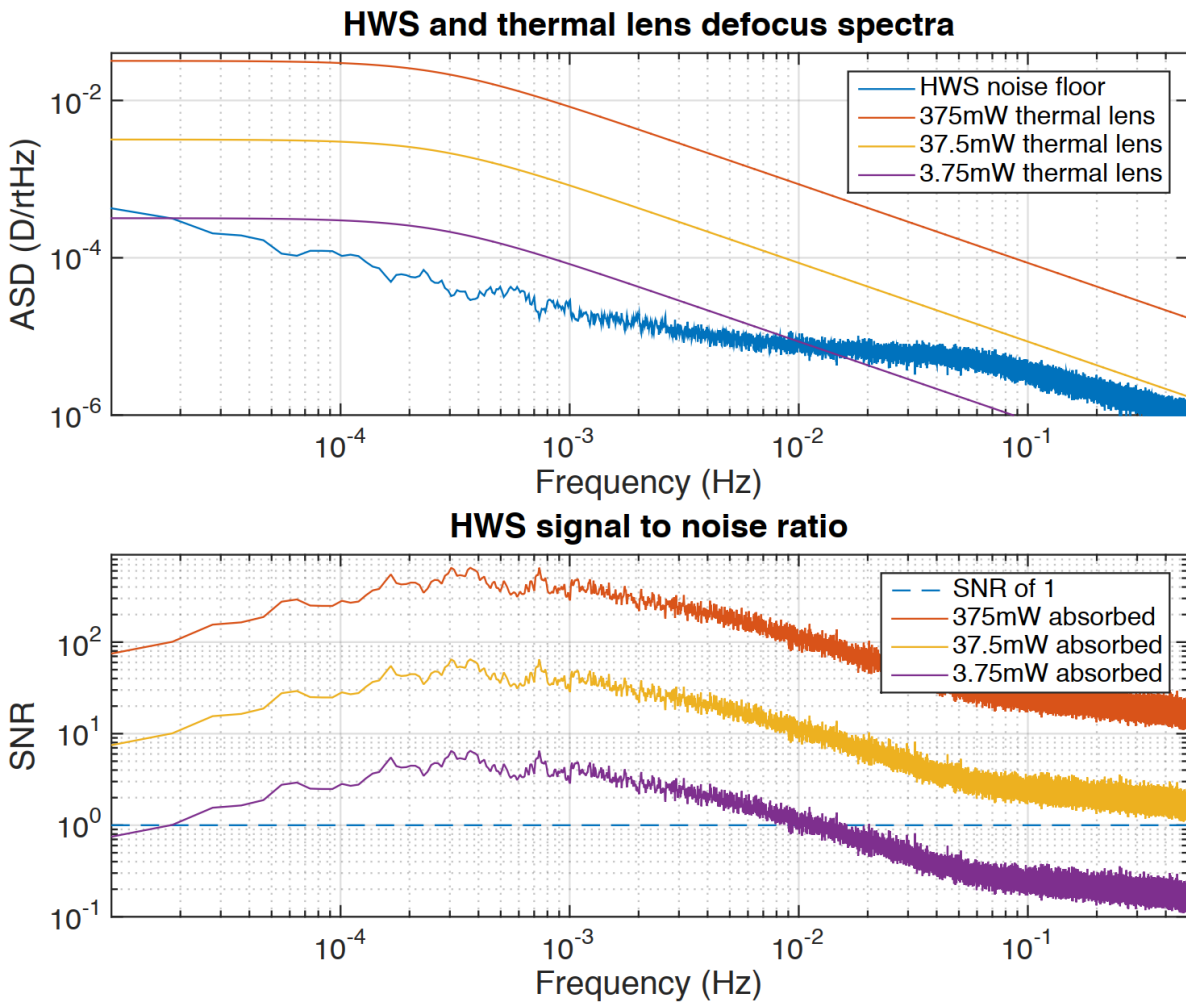
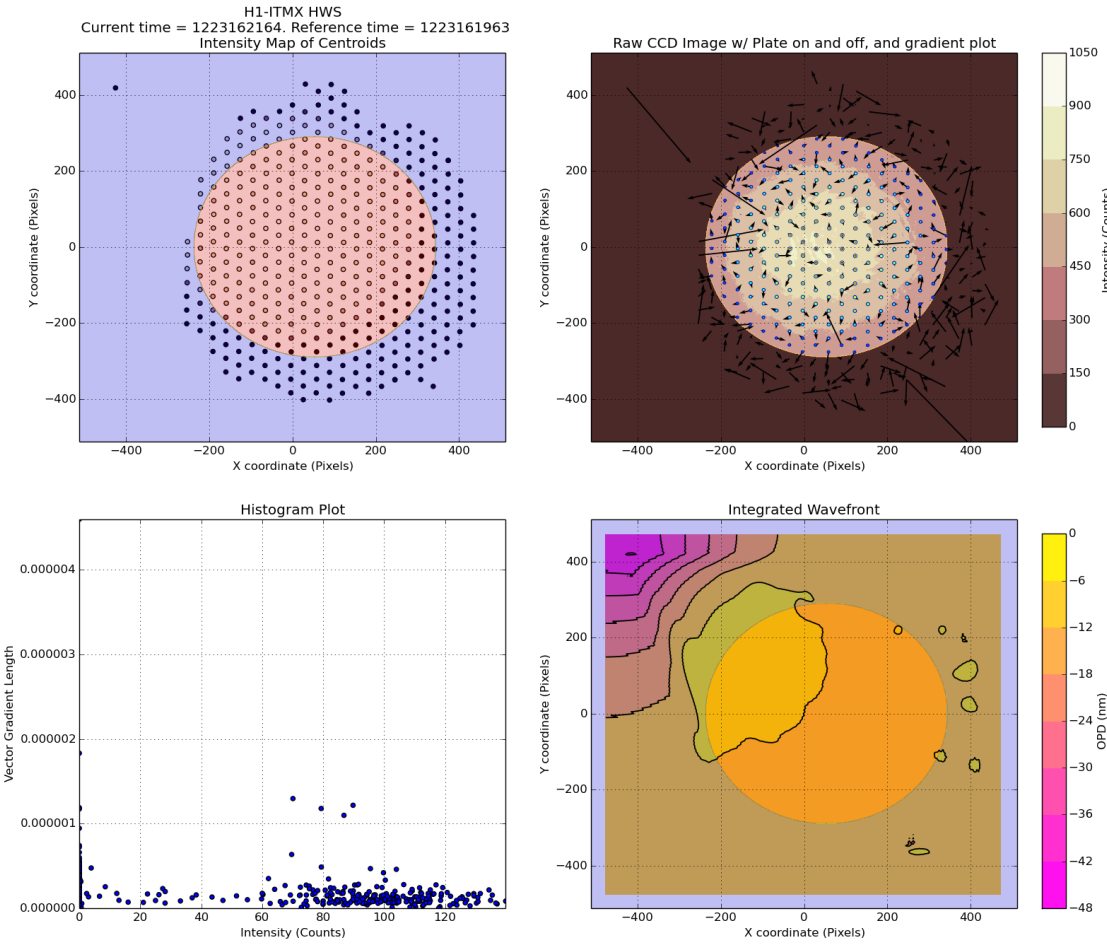


Figure 1.5: **Noise spectra for the HWS spherical lensing.** Taken from [17], this puts a lower bound on the Hartmann sensitivity to distortions for various time scales.



**Figure 1.6: ITMX Hartmann Sensor output.** Between the reference and current times for this measurement, no heating was applied to the test masses so the expectation is a relatively flat and smooth wavefront. This is mostly true except for a large, anomalous arrow at pixel coordinate  $[X, Y] = [-410, 405]$  of the gradient plots (upper right) which leads to a false wavefront distortion in the same area for the contour plot (lower right). The sharp iris in the middle represents a digital mask that is can be turned on to reduce the effects of fringing. A histogram in the bottom left plot shows the intensity distribution for each of the gradients; if the HWS beams are co-aligned well with the interferometer beam, then most of the information about thermal lensing occurs near the center of the intensity distribution.

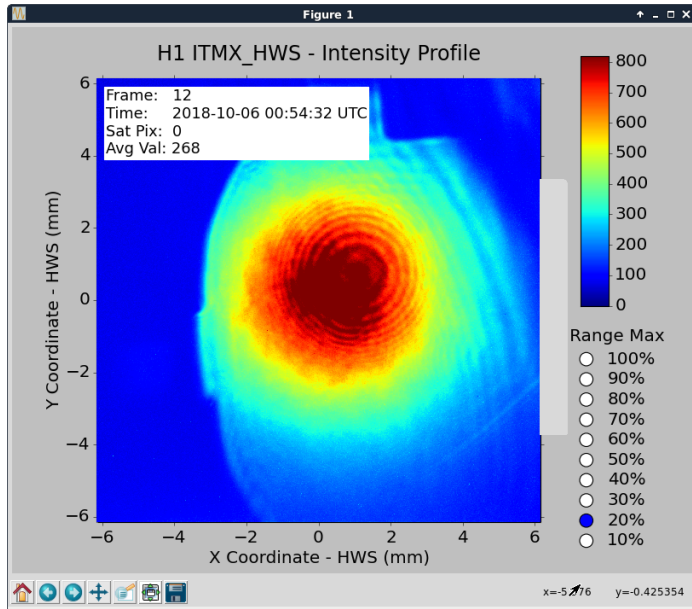


Figure 1.7: Clipping on ITMX Hartmann Sensor.

references to find the average of surrounding pixels and replace the problematic pixel. This digital procedure greatly reduced the amount of glitches found in the Hartmann sensor data.

When increasing the input power into the interferometer, there were large spikes associated with the spherical power estimation on the ITMX. This was eventually tracked down to leakage beam introduced by stray light from the interferometer. At times, the leakage beam was 40% the intensity of the main Hartmann beam which severely distorted the fitting algorithms. ITMY HWS did not see this effect because SR2 is such a good high reflector and attenuated any 1064 nm contributions down to the PPM level.

### Measuring Uniform Absorption

After the arm power drops suddenly, the heat decays exponentially depending on the amount of absorption on the high reflective surface of the arm cavity. Using the HWS, it is possible to fit the decay rate to a finite element model of a cylindrical mass. A fitted parameter for absorption is extremely important in pre-determining the amount compensation necessary to prepare the test masses for lock acquisition.

Applying a Markov Chain Monte-Carlo method allows some statistical uncertainty es-

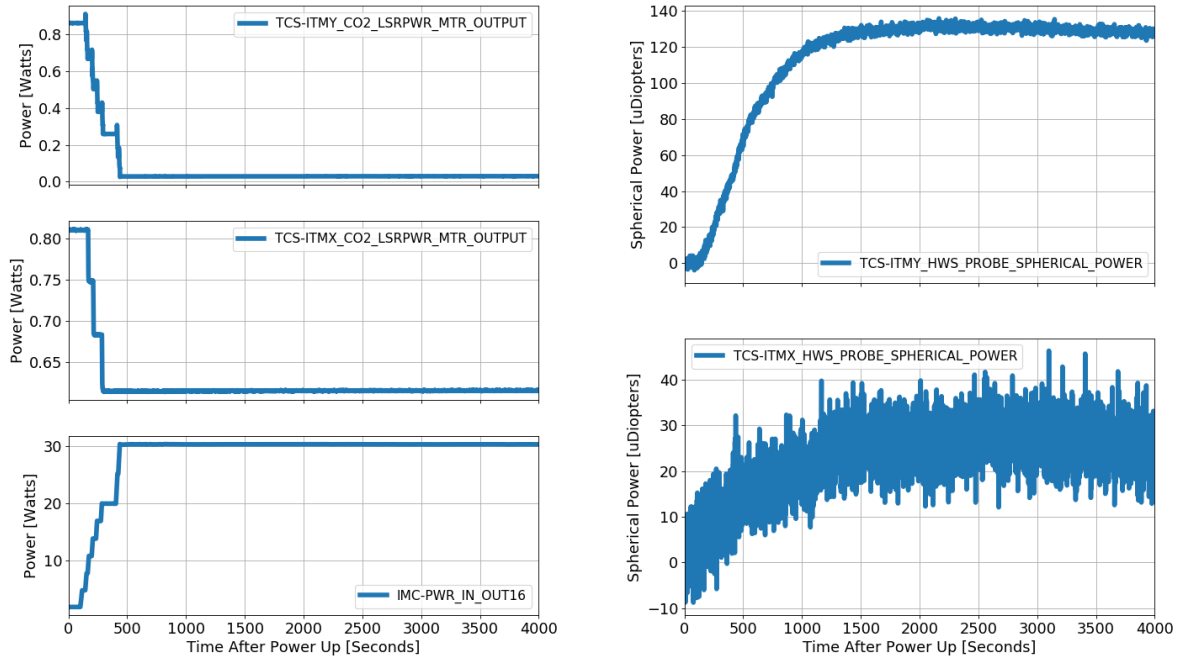
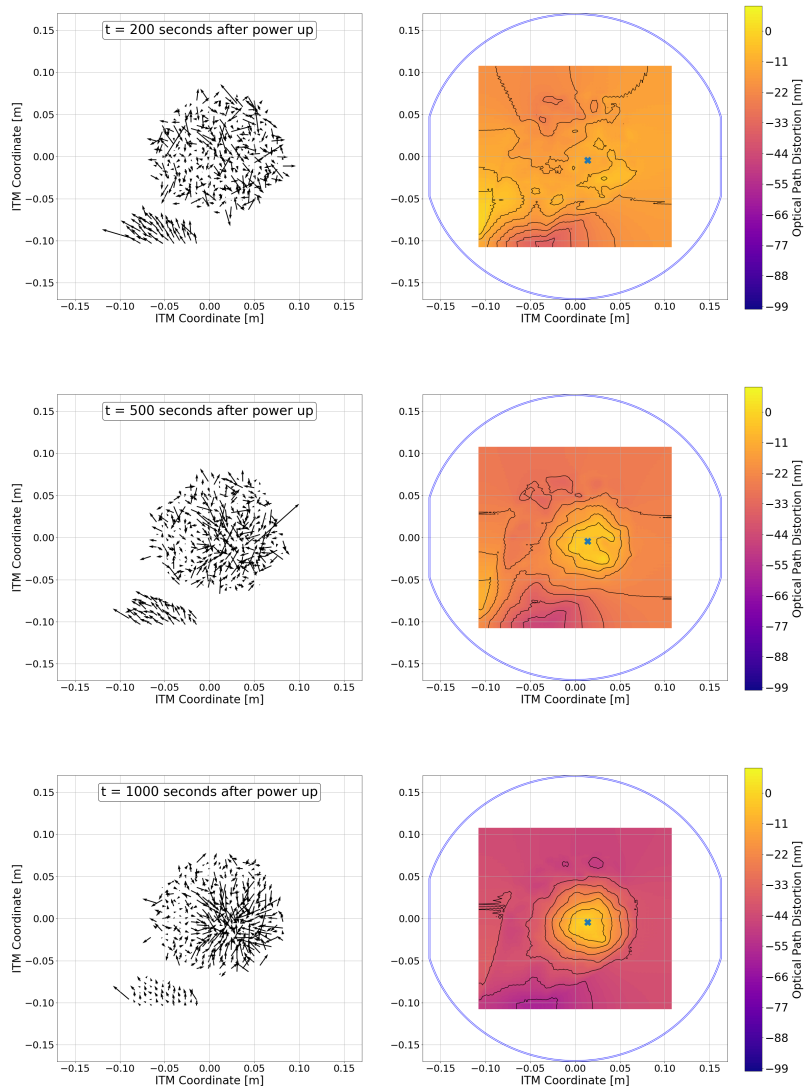
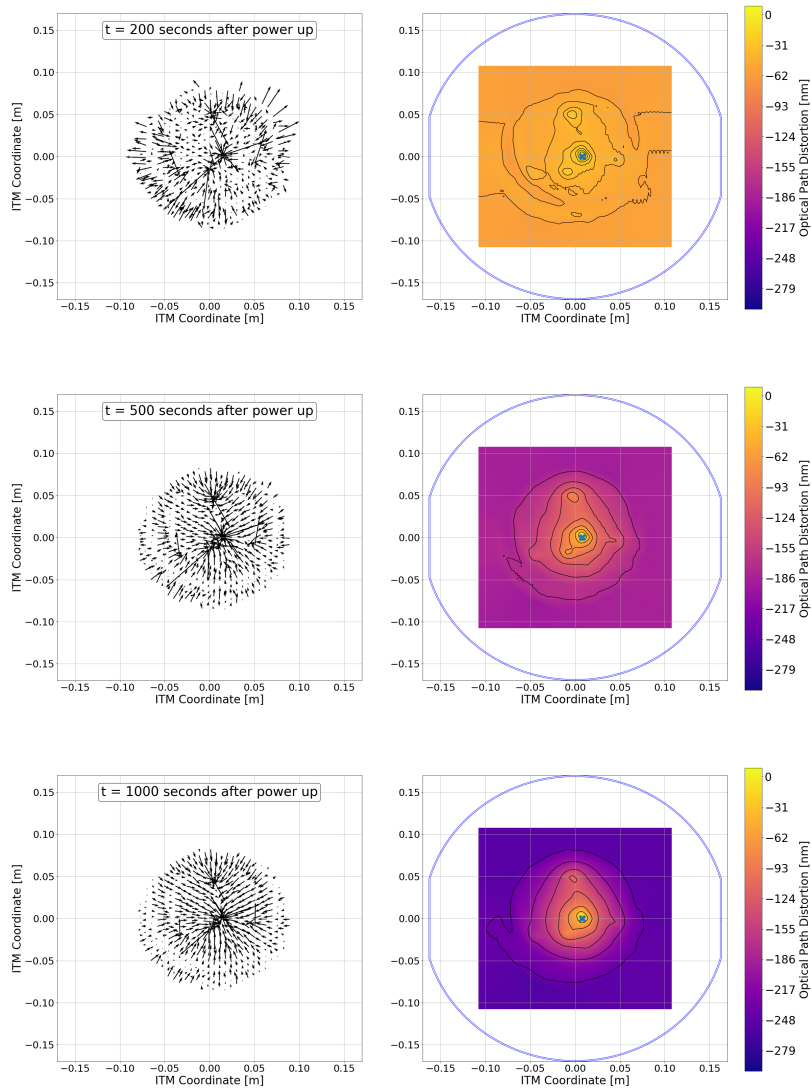


Figure 1.8: **A time series of the interferometer power increase sequence.** During this time, the interferometer is using DC-readout and locked at 2 watts of PSL input power with all of the angular control loops closed with high-bandwidth, in this configuration, the power recycling gain is approximately 45. The left figure shows the increase of PSL input power and the CO<sub>2</sub> lasers stepping down in power where levels of compensation were experimentally determined such that the angular control loops were stable and sideband build ups remained as high as possible. The right plot shows the Hartmann sensor spherical power as a function of time with the starting point scaled to zero micro-diopters. Although the point absorbers do not exhibit the same spatial structure as uniform heating so it is difficult to derive absolute absorption for ITMY, the spherical fitting gives some information about the relative scale of heating absorption between the two optics.

timates for the exponential fitting to the data shown in Figure 1.12, where the priors are assumed to be random Gaussian noise and the initial guesses are scaled roughly with a least squares fitting algorithm. Figure 1.11 shows the measured spherical power from interferometer heating for ITMX/ITMY and comparing the two optics shows that the spherical power difference for ITMY is almost a factor of 2 larger than ITMX. One of the main differences



**Figure 1.9: ITMX gradient plots (left) and wavefront maps (right) during a power up to 30 Watts of input power.** It is important to note that there is a back-reflected stray beam from the super-luminous LED that is incident in the bottom left portion of the camera which is digitally cropped out during the real-time analysis. As previously noted, this particular Hartmann sensors suffers from beam clipping on the right side of the image which adds to the systematic noise. A blue cross denotes the origin which is fitted with the Zernike polynomials to derive a spherical power. The arrow lengths in the gradient plots are normalized to each individual plot and are meant to guide the eye in discerning the directionality and pattern of lensing.



**Figure 1.10: ITMY gradient plots (left) and wavefront maps (right) during a power up to 30 Watts of input power.** Compared to the ITMX phase map in Figure 1.9, ITMY has a much larger overall heating pattern and higher spatial frequencies in the contours which was the first clue that revealed multiple (possibly 4) point absorber on the test mass. There is also a halo of gradients on the outer rim of the plots which is most prominent on the lower left corner. This is due reducing the CO<sub>2</sub> laser power in an attempt to compensate the lensing effects as the interferometer beam heats up the test mass. The overall scale of self-heating with the higher spatial frequencies of the point absorbers makes it incredibly difficult to compensate with using the CO<sub>2</sub> lasers as designed by Advanced LIGO.

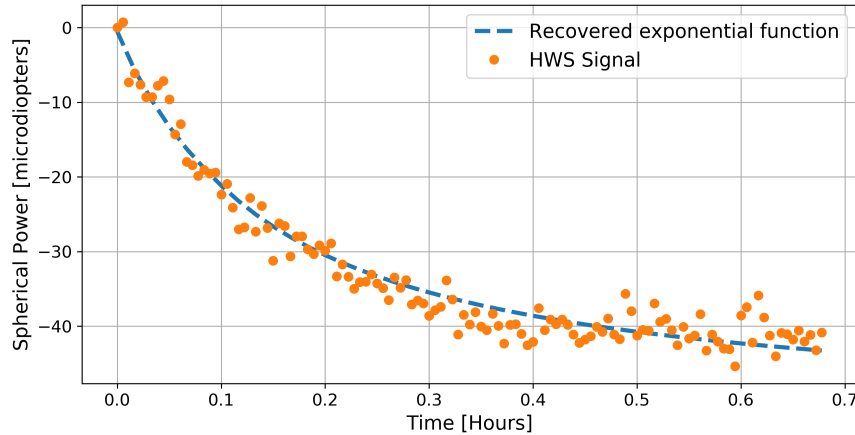
between the O2 and O3 observing runs was the replacement of ITMX, ETMX, and ETMY test masses. With a fully running Hartmann Sensor system in place which monitors the wavefront curvature across the optic, long-term trends over the observation runs will be able to determine how absorption changes as a function of time and whether test masses have an innate lifetime. This will be particularly important if the next generation of detectors use much higher power levels in order to achieve better high frequency sensitivity [18]. Using this method, the current absorption estimates for the H1 input test masses are as follows:

$$\begin{aligned} A_{\text{ITMX}} &= 328 \pm 84 \text{ ppb} \\ A_{\text{ITMY}} &= 688 \pm 85 \text{ ppb} \end{aligned} \tag{1.32}$$

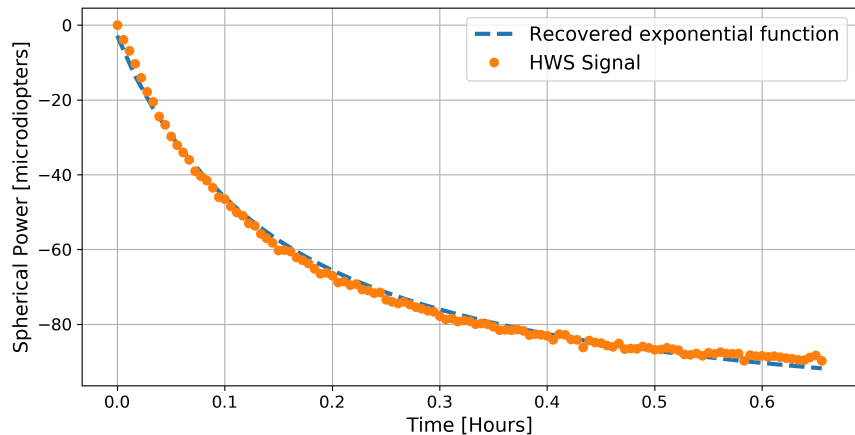
### 1.4.2 Ring Heater and CO2 Commissioning

To counteract the effects of interferometer heating, Advanced LIGO uses a ring heater [73] [86] which has two heating elements mounted on the suspension cage. Each of them are glass formers wrapped by nichrome wire that has current running through it and radiates an annular heating pattern. The ring heaters will have two effects, it will induce a substrate lens and a radius of curvature change. As shown in Section 1.1, the carrier beam will not see the substrate lens but the radius of curvature difference will change the overall modal shape of the cavity. Similar to the distortion derived in section 1.2 where the thermo-refractive effect dominates when dealing with a Gaussian beam, the same is true from the ring heaters. Using equation ??, one can directly calculate the power overlap between a pre-loaded cavity and the original, as it turns out, the effect varies the overlap by less than 0.1%

After using the Hartmann sensors to determine the absorption and pre-loading the ring heaters to compensate the interferometer lensing, the substrate is no longer in the nominal configuration during lock acquisition. Therefore, it is necessary to use CO2 (Carbon Dioxide) lasers to mimic the interferometer's heating on the compensation plate. The CO2 lasers



(a) ITMX absorption



(b) ITMY absorption

**Figure 1.11: Thermal lensing as seen by the ITM Hartmann Sensors after a lock loss.** A finite element simulation from COMSOL shows an impulse response which resembles an exponential decay can be linearized and fitted to the spherical power. The model assumes a beam size of 54 mm and 1 Watt of uniformly absorbed power then uses MCMC to fit the offset and scale to the data. Comparing ITMX and ITMY at Hanford shows a huge overall difference between the two optics, mostly due to the fact that ITMY has multiple point absorbers adding to the absorption estimate. In addition, fitting ITMY data points with the model does not seem to agree very well which indicates extra physics that stems from non-uniform heating by a 54 mm beam.

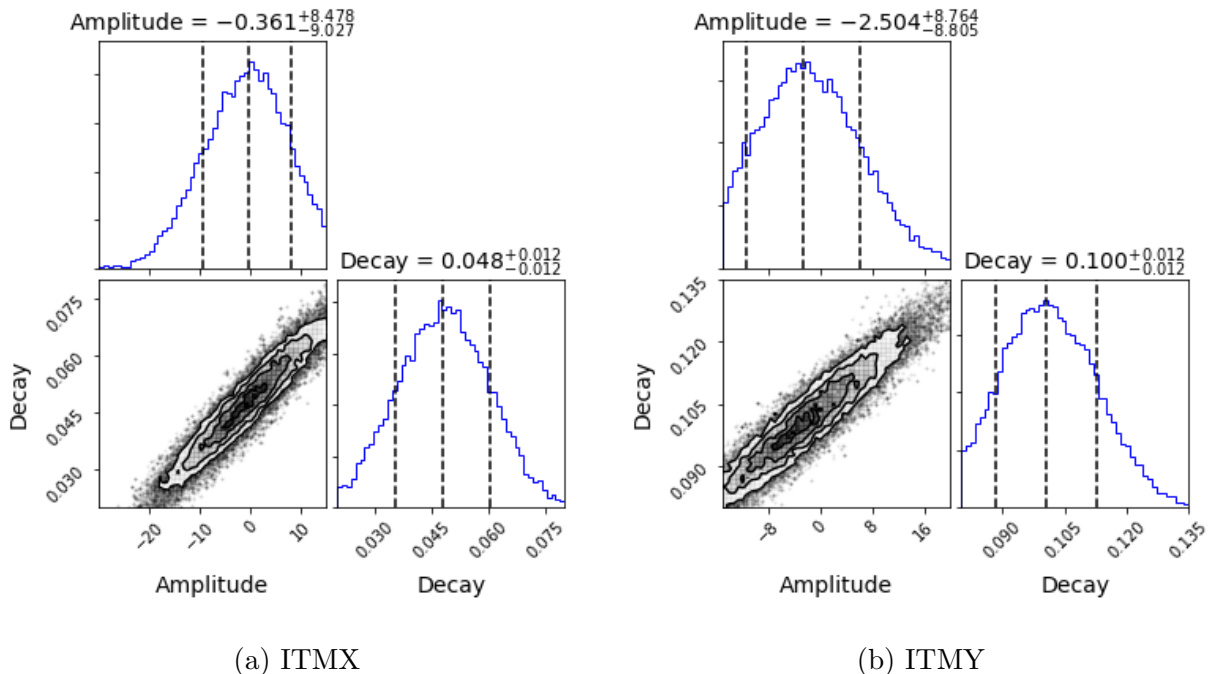


Figure 1.12: Posterior distributions from fitting the Hartmann sensor spherical power. Using the MCMC Hammer [42]

are located on each input test mass chamber and injected through a double zinc selenide viewport, then two steering mirrors direct the heating beam on the compensation plate of the reaction mass. In initial LIGO, the CO<sub>2</sub> beams were injected onto the high reflectivity surfaces of the test masses which created both a radius of curvature on the cavity side and a thermo-refractive change in the substrate. However, in advanced LIGO, the CO<sub>2</sub> lasers will only affect the substrate lensing. Tuning the CO<sub>2</sub> power will have a dramatic effect on the interferometer auxiliary degrees of freedom because the sidebands get rejected by the arm cavity and only resonate in the recycling cavities.

The self-heating caused by the interferometer beam is assumed to have a Gaussian intensity profile, while the CO<sub>2</sub> heating beam is meant to have a uniform heating profile across the test mass surface which allows for a consistent phase distortion as a beam passes through the substrate.

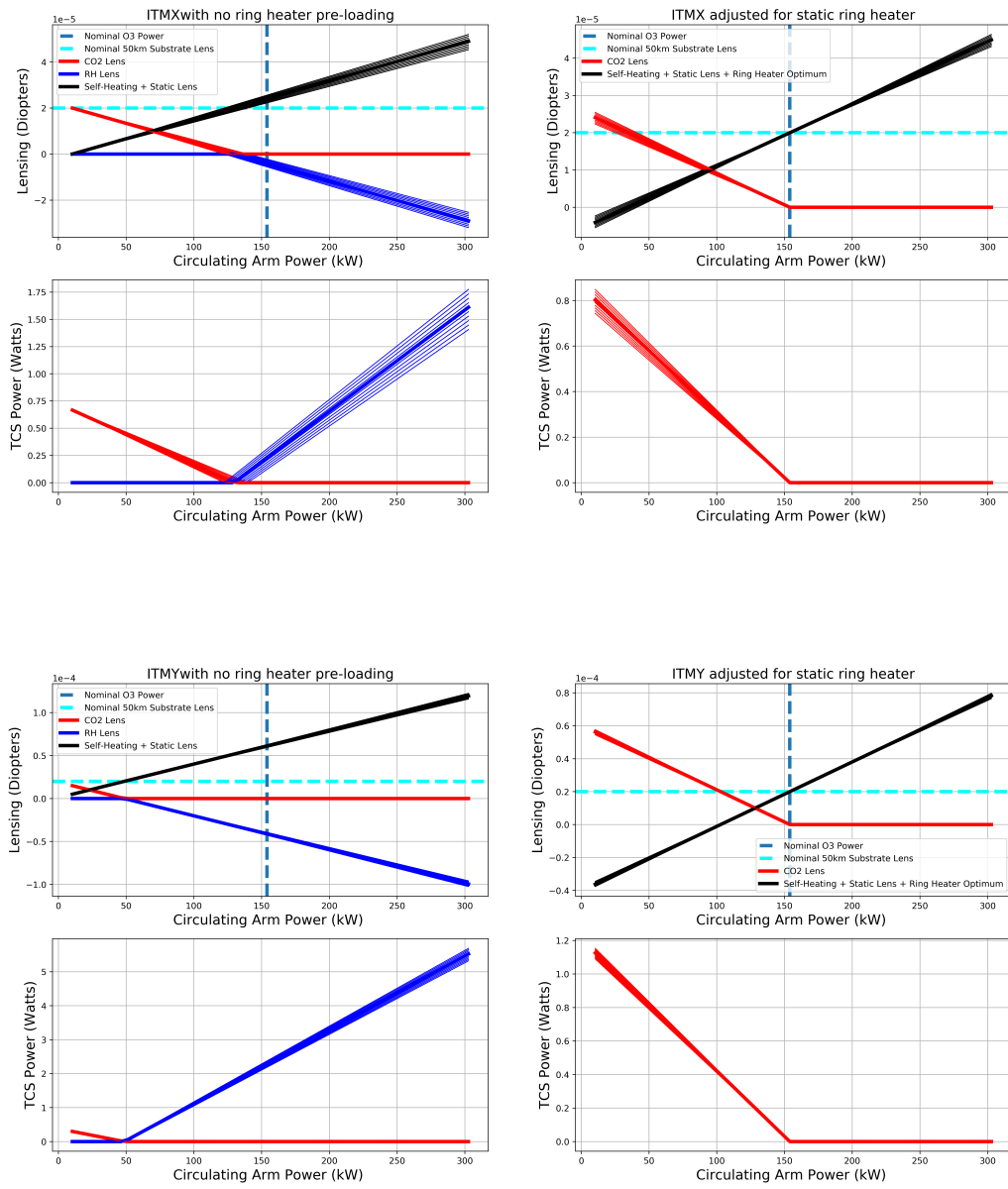
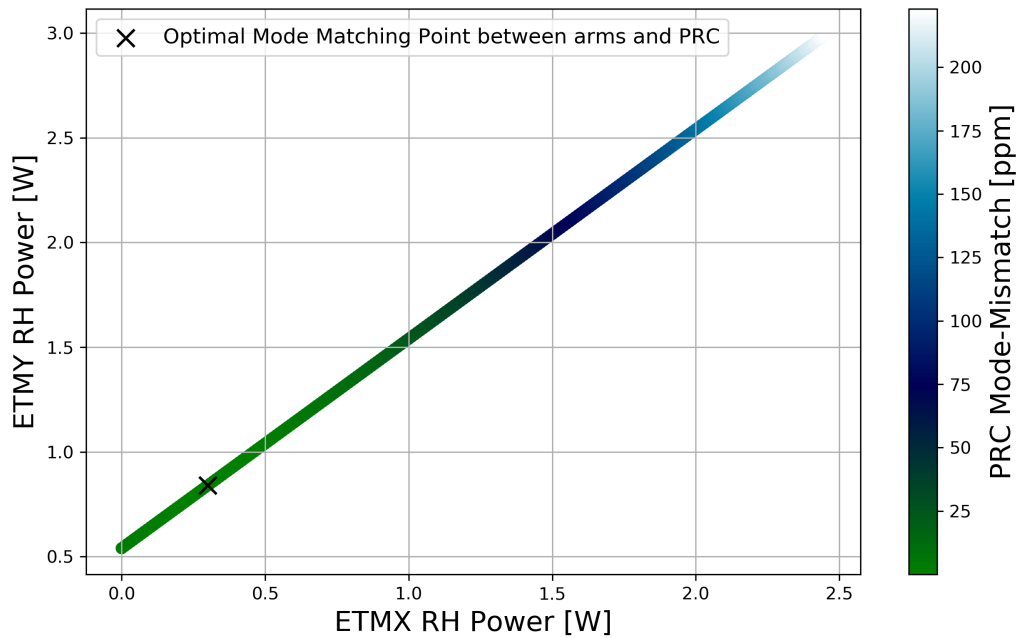


Figure 1.13: **Calculated TCS settings to balance the substrate lens.** The nominal circulating power denoted by the vertical blue line is a function of the input power, the recycling gain, and the arm cavity gain. The nominal input power for O3 will be 50 Watts and the power recycling gain is around 45. The arm cavity gain can be estimated by calibrating the transmitted power from each of the arms and is approximately 228. The horizontal, dashed turquoise line represents the nominal substrate lens with a focal length of 50 km. This value is what the power recycling cavity expects to properly mode match to the arms.



**Figure 1.14: Mode matching the arm cavities to the power recycling cavity.** Determining the ITM ring heaters and CO<sub>2</sub> power levels still leaves the end test mass ring heaters to be set. The goal is to maintain the mode matching between the arms while simultaneously searching for the optimal overlap with the power recycling cavity. This is done by determining the spatial mode overlap between all three cavities (2 ARMS) The linear portion of the graph shows a combination of common and differential adjustment of each ring heater that keeps the mode matching between the arms at less than 1 PPM

	Substrate	HR surface	Compensation Plate
Self Heating	*4.9e-4	*-3.6e-5	N/A
Ring Heater	-9.0e-6	*9.9e-7	N/A
CO2x	N/A	N/A	1.5e-5
CO2y	N/A	N/A	2.5e-5

Table 1.1: **Single pass actuator lensing calibrations for aLIGO TCS in micro-diopters/Watt.** The asterisks indicate the values are extracted from a model and the measured values use the Hartmann sensors which cannot distinguish between surface and substrate lensing, however, the latter is larger by an order of magnitude. CO2x and CO2y were measured to be different in their actuation strength which could stem from either misalignment or a misplaced central mask. The uncertainty is expressed by the last digit available.

## 1.5 Point Absorbers

Up till to point, all actuators models, and measurements assumed uniform absorption across the optics which results in second order Hermite-Gauss coupling with the fundamental Gaussian beam . As it turns out, this assumption is not so simple. One of the main successes for the Hartmann Wavefront Sensors have been the ability to find excess absorption due to point absorbers on the high reflectivity surfaces of the test masses. During the second observation run (O2), there was an absorber found on ITMX that made increasing the input power past 30 watts extremely difficult and futile because it was thought to couple intensity noise into DARM. The exact origin of these point absorbers is still an active area of research but incursions into the vacuum system will always pose a risk of spreading particulate on the HR surfaces.

*Part way into commissioning for O3, another point absorber on ITMY was detected that showed similar characteristics.* Since their spatial frequencies are much higher than the uniform absorption, many of the models for scattered power and thermal effects require significant adjustment to predict the interferometer behavior. To decompose the differential phase map into the Hermite Gauss basis requires a relatively high order and makes full interferometer simulations very difficult. For example, FINESSE

calculations on a laptop tend to become unwieldy at around  $n + m \leq 6$ . This affects the HWS's ability to properly evaluate total thermal lens from the interferometer, therefore changing the estimated absorption. There are two main parts which allow point absorbers to adversely affect interferometer performance. The first is scattering from the arm cavity that takes away carrier light and couples to higher order modes, and secondly, the thermal lens in the substrate distorts the power recycling cavity for the sideband build ups dramatically.

A few ways to try getting around this could be separating the temporal effects which quadratically depend on the point absorber size. The thermo-refractive transient solution found in Vinet [85] has the form

$$Z_{\text{TR}}(t) \propto 1 - \exp\{-t/\tau\} \quad (1.33)$$

where  $\tau = \frac{\rho C w_{\text{pa}}^2}{3\kappa}$  is the characteristic time constant that depends on the beam size  $w_{\text{pa}}$ , the thermal conductivity  $\kappa$ , the specific heat  $C$  and the material density  $\rho$ . A simple model can consist of two beams with different sizes which will have separate time constants. Another interesting way of characterizing what can be compensated for O3 could be to Fourier transform the optical path distortion and low pass the high spatial frequency components with a Gaussian filter. The cut-off frequency can be estimated by the approximate point absorber size (10-20 mm). Of course, early detection and replacement of an optic may be the most efficient way to avoid custom thermal compensation. Figure 1.15 shows a comparison between ITMX and ITMY while the interferometer is increasing input laser power from 2 to 30 Watts. Within the first few hundred seconds, the point absorbers begin showing up in the optical path distortion map.

During commissioning periods, the highest starting priority is to achieve full resonance as quickly as possible and is easier with approximately 2 Watts of input laser power. This requires locking the arm length stabilization (ALS) system with 532 nm, the vertex degrees of freedom (DRMI) and complete the common arm length (CARM) transition. Additionally,

closing all angular degrees of freedom (ASC) will take a lot of time and energy. If major upgrades or fixes have occurred such as replacing main test masses then all the prior steps require many months of commissioning. Generally, vacuum incursions into the main vertex cost the most time and money because of the large volume needing to be pumped. All this is to say, the earlier point absorbers are detected, the better. However, this requires a high level of arm power which historically has come much later on the road to nominal low noise. In Figure 1.5, the signal-to-noise ratio is 10 at 0.01 Hz for 37.5 mW of absorbed power which means the circulating arm power must reach at least 75 kW (assuming absorption is approximately 0.5 ppm) to be detectable within the time constant of point absorbers. This could still be achieved without full lock if the first priority after pumping down is resonating a single arm with power recycling at the highest input laser power possible (currently 70 Watts). With a single power recycled arm cavity the expected circulating power absorbed on the HR surface of the test masses is

$$\begin{aligned} P_{\text{PRC-1ARM}} &= P_{\text{in}} * g_{\text{PRC}} * g_{\text{ARM}} * 0.25 * \epsilon_a \\ &\approx 98 \text{ mW} \left[ \frac{P_{\text{in}}}{70 \text{ Watts}} \right] \left[ \frac{g_{\text{PRC}}}{45} \right] \left[ \frac{g_{\text{ARM}}}{225} \right] \left[ \frac{\epsilon_a}{0.5 \text{ ppm}} \right] \end{aligned} \quad (1.34)$$

where the factor of 0.25 comes from double passing the main beamsplitter, the coefficient  $\epsilon_a$  is the estimated uniform absorption. Using  $D_{\text{sub}} \approx 487 \frac{\mu\text{D}}{1 \text{ Watt}}$  as the modeled conversion from absorbed power to steady-state spherical power, the expected substrate lensing in units of micro-diopters [ $\mu\text{D}$ ] is

$$S_{\text{PRC-1ARM}} = P_{\text{PRC-1ARM}} * D_{\text{sub}} \approx 48 \mu\text{D} \quad (1.35)$$

which is readily detectable by the current Hartmann sensors. Commissioning and installation schedules are ever-changing entities and there have been times when the end stations are not ready for integration simultaneously. This provides a window where only single arm commissioning is available so this method might be able to detect the existence of point

absorbers much sooner.

Once these anomalies are found, the question remains, what can be done?

One consideration is a complete re-design of Thermal Compensation to account for higher frequency spatial corrections. There are already custom masks at Hanford which are designed to smooth the optical path distortion in the substrate and can be implemented with the CO<sub>2</sub> lasers on the compensation plate to increase the sideband build ups, which is one of the biggest difficulties associated with point absorbers. However, this does not solve the fundamental problem of losing power recycling gain due to power scattering where the quadratic losses of the arm cavity set an upper limit for increasing power. Another way to avoid these effects is to move the beam spot away from the point absorber on the HR surface but it must be sufficiently far or the odd higher order modes will couple very strongly with asymmetry.

## 1.6 Higher Power Operation

The goal for O3 is at least 150 kW of circulating power in the arms.

With the sensors and tests described in the preceding sections, a cohesive plan to pre-load the interferometer was implemented in order to achieve stable higher power operation in the detectors. Generally, the Thermal Compensation System has two goals: Firstly, the actuators are used to pre-load the test masses with heat in anticipation of the lensing due to the interferometer while operating at full lock and higher power. Secondly, the amount of mode-matching between the coupled cavities must be optimized in order to achieve the best sensitivity. Using the absorptions measured in Figure 1.11, it is possible to estimate the total amount of lensing from self-heating as a function of input power.

In principle, the Hartmann measurements of absorbed power provide sufficient information to pre-loaded the interferometer in anticipation of 50 Watts of input power. At Hanford, this proved to be very difficult for reliably locking the interferometer, so with the combi-

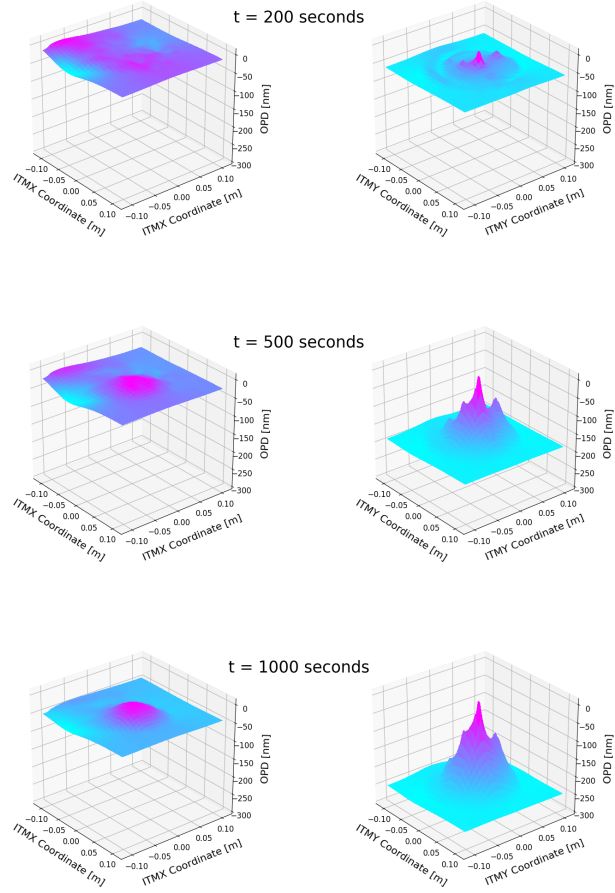


**Figure 1.15: Comparing 3-D plots of the optical path distortion for ITMX and ITMY test masses after powering up the interferometer.** The horizontal axes represent the test mass coordinates as seen on the Hartmann sensors and the vertical axis is the optical path distortion in units of nanometers. The color map is scaled for each plot and is meant to show particularly hot areas and roughly compare the high frequency spatial distribution of point absorbers. Plots in the left column (ITMX) have smooth spatial features that stem from uniform absorption and the effects are not prominent till after approximately 500 seconds. In contrast, plots in the right column (ITMY) have very sharp spatial features which already rise above the floor at 200 seconds into powering up. Comparing the overall surface deformation on the same scale, the difference between ITMX and ITMY is striking and it is clear how an interferometer with point absorbers on the surface will struggle to increase powers above 200 kW within the arm cavities.

nation of estimates provided by the Hartmann Sensors and experimentation with the CO2 power levels at each stage of increasing the PSL power, we are able to consistently lock at 30 Watts of PSL input power and  $\approx 140 \text{ kW}$  of circulating arm power. The biggest difficulty associated with implementing this thermal compensation scheme was consistently locking DRMI in high micro-seismic conditions. This could be contributed to misalignment of CO2 lasers to the test masses, which were initially aligned using the Hartmann sensors and double-checked by cycling the lasers on/off to measure the single bounce interferometer beam deflection at the anti-symmetric port.

This required considerable tuning of the thermal compensation system that is not needed at Livingston for the same input power. Although both interferometers saw a decay in power recycling which was found to be attributed to a point absorber on L1-ETMX.

During the early phases of commissioning higher power at Hanford, most of the locklosses occurred when the 9 Mhz sidebands would fall below a certain threshold level.

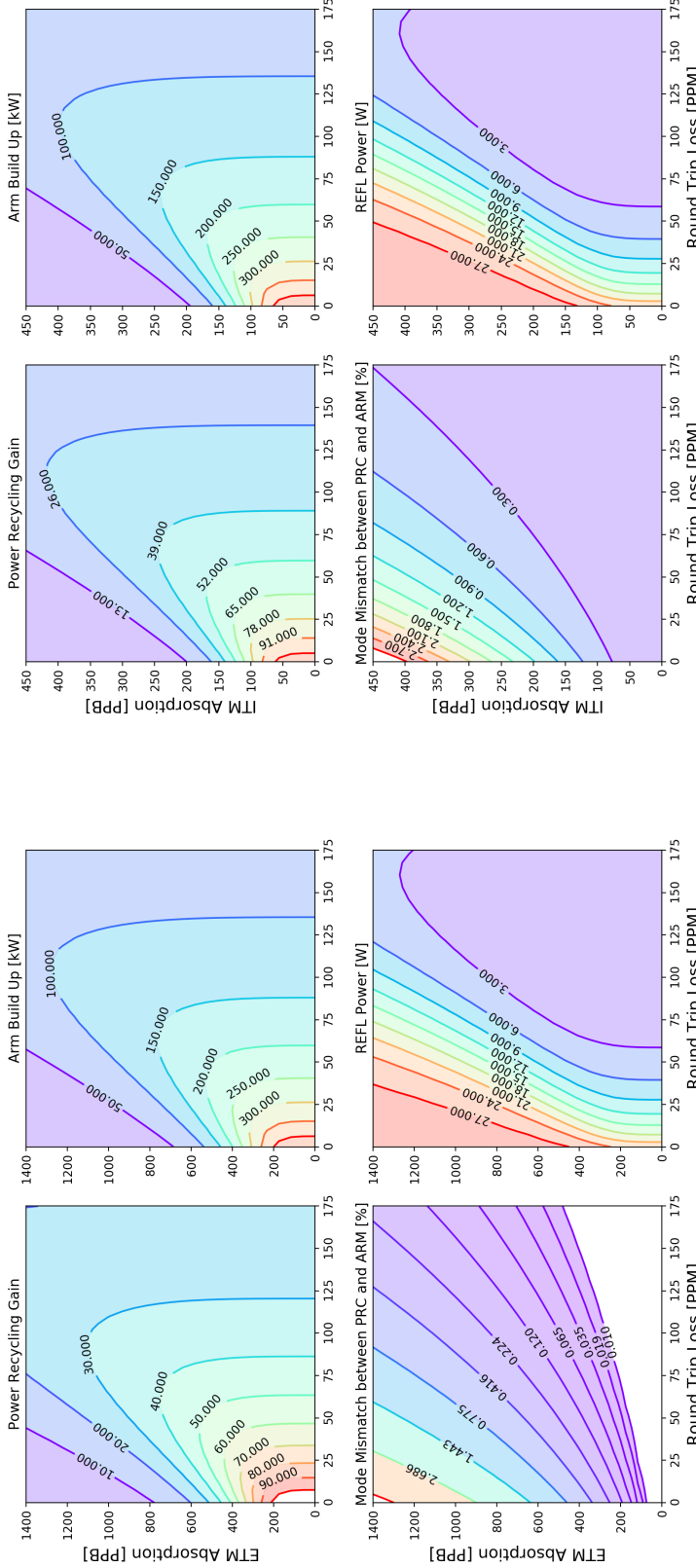


Figure 1.16: **Interferometer DC powers as a function of round trip arm loss and test mass absorption.** Simplifying the power recycling cavity and a combined arm model to understand the powers as a function of loss has a few advantages with regards to computational time and the results are easier to conceptually understand. Here, absorption changes the radius of curvature and substrate thermal lens which results in some mode mismatch while the round trip loss takes into account the rest of the higher order modes from point absorbers. The ITM absorption has a much larger effect on the overall power recycling gain loss by almost a factor of 3 compared to ETM absorption. Of course, the simplified model will fall short in describing effects on the antisymmetric signals of the full interferometer.

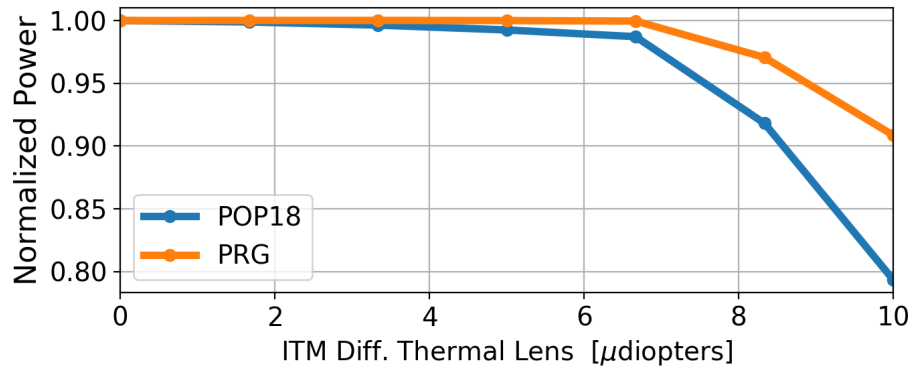


Figure 1.17: **Model of POP-18 as a function of differential thermal lensing using FINESSE.** The horizontal axis is differential lensing between the ITMX/ITMY substrates and the vertical axis represents the normalized power when locked with nominal mode matching. POP-18 is the signal at the power recycling pick-off port demodulated at 18 MHz which shows the sideband power buildup in the power recycling cavity. In this particular simulation the differential lensing requires finding a new operational point to lock the longitudinal degrees of freedom. Additionally, the sensors which are used to maintain resonance and readout the RF power need to be re-phased in order to get the upper limit estimate. Even with modest differential lensing (10 micro diopters), the buildup drops by 20 percent and eventually the simulation has trouble maintaining resonance similarly to the actual interferometer.

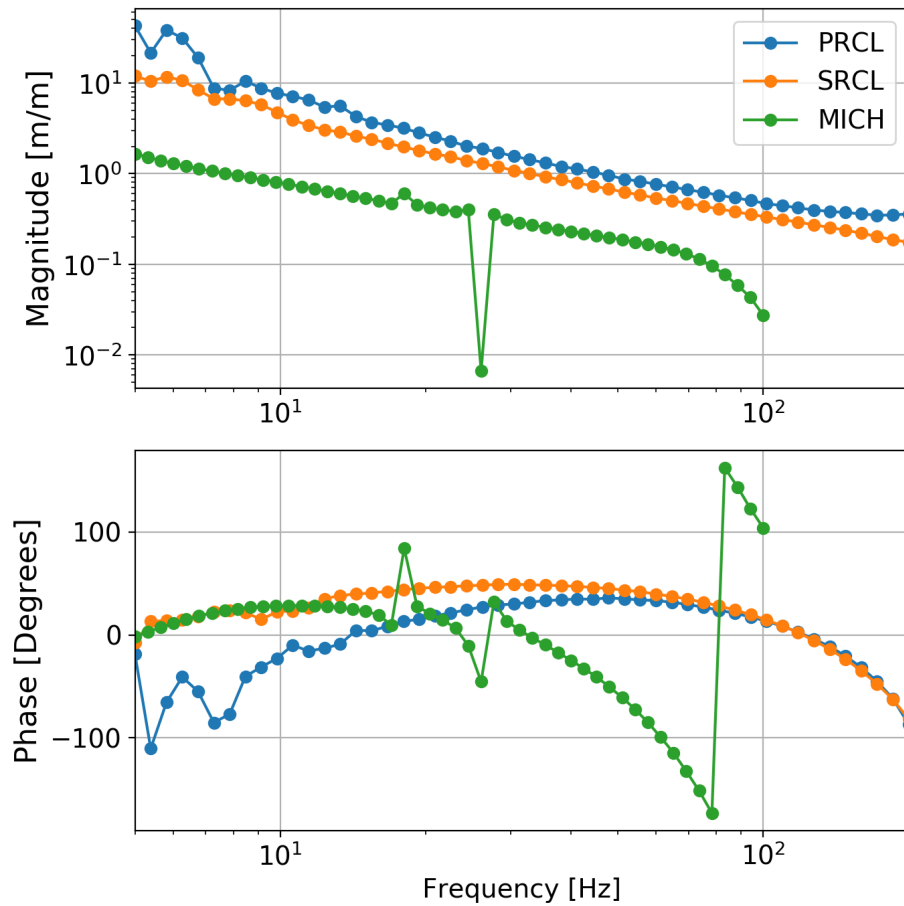


Figure 1.18: **Vertex open loop transfer functions while in Nominal Low Noise.** The nominal UGF for PRCL is around 45 Hz.

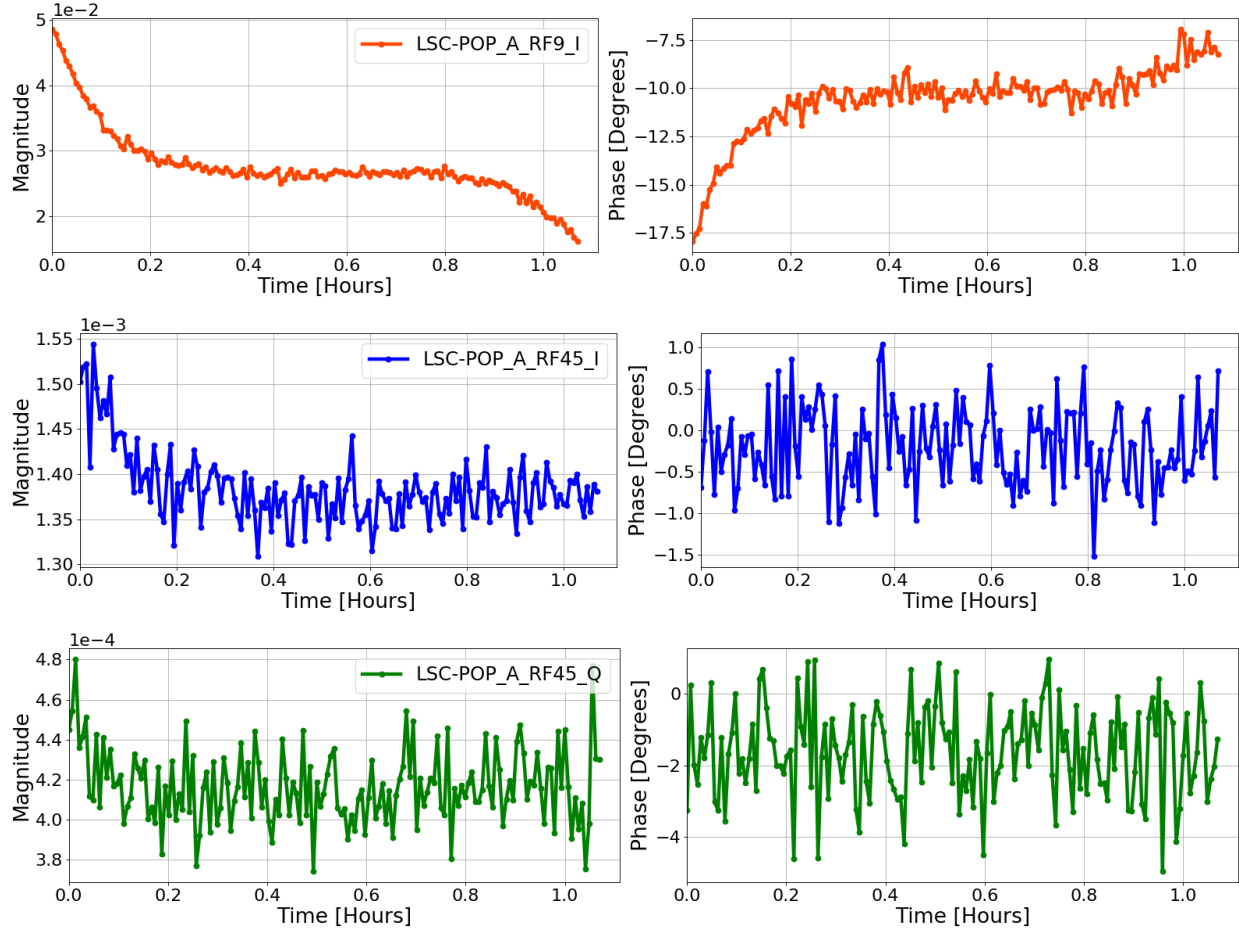


Figure 1.19: **Measuring vertex optical gains as a function of heating.** Injecting a dither line into each degree of freedom and digitally demodulating the respective sensors at the excitation frequency can provide insight on how much the optical gain/phase shifts as a function of heating. At time  $t=0$ , the power begins increasing from 2 watts of input power to 20 watts. In PRCL, there is a reduction to 80% of the starting magnitude and 7.5 degrees of phase rotation with the first power increase. At 0.9 hours, the input power goes from 20 to 30 watts and the magnitude drops to about 30% of the original gain which results in a lock loss. As for the SRCL and MICH degrees of freedom, there are slight changes first power increase but not nearly as bad as PRCL.

## 1.7 Mode Matching from the OPO to the OMC

Using the OMC as an optical spectrum analyzer is one simplest methods for understanding the mode matching coming out of the interferometer. In the single bounce configuration, measuring the ratio between the second order mode and the fundamental gives a first look at the limit of matching. The same can be done using the squeezed beam as well and during commissioning of the squeezer, a mode mismatch of 16% was observed which led to a re-design of the OPO to OMC optical path.

Using a well-calibrated mode profiler that measures beam sizes along the propagation axis is the most direct way of determining OPO to OMC mode matching. This method can also predict the actuator Gouy phase of the second lens after the OPO, which is on a translation stage with approximately 4 centimeters of range. Generally, the length measurement between

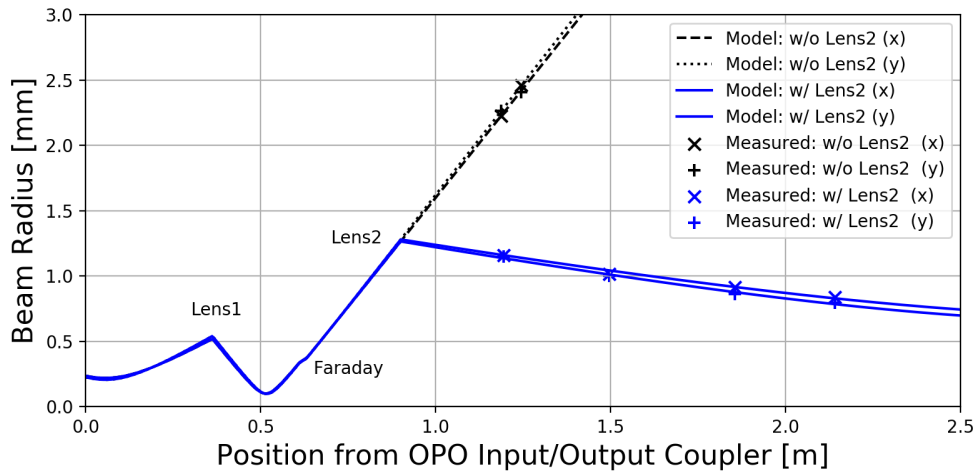
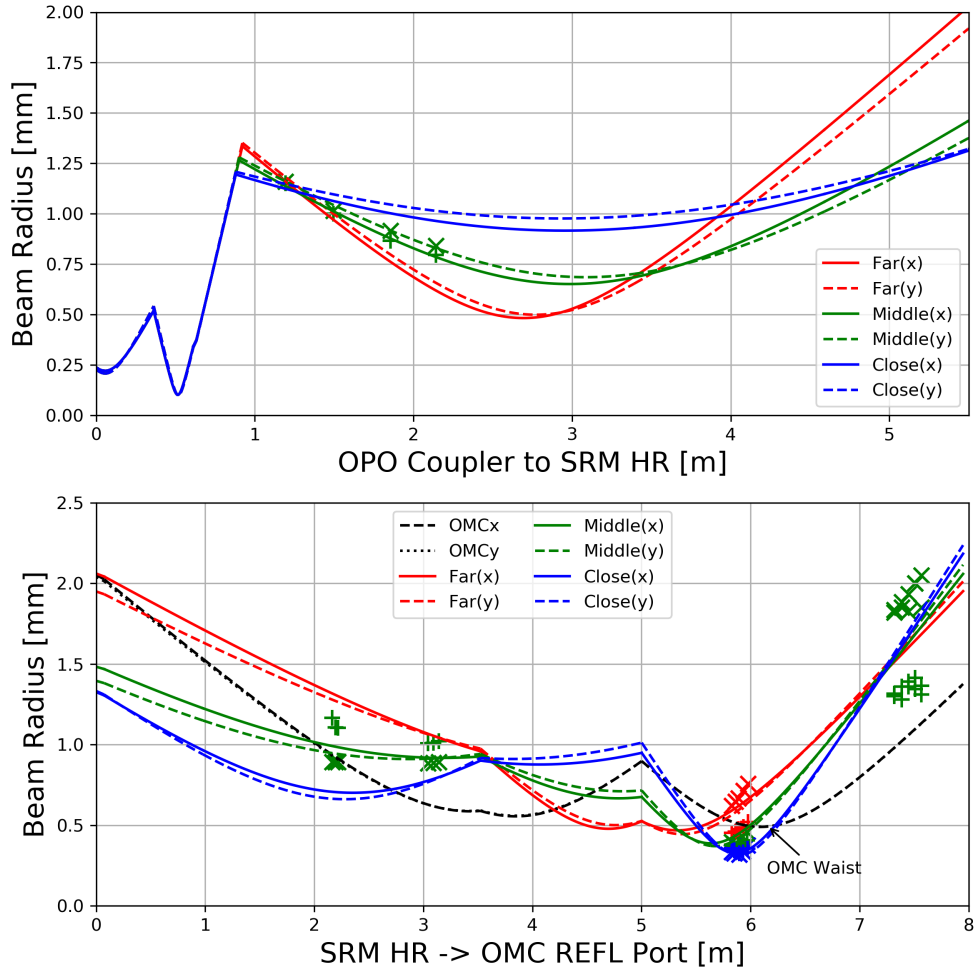
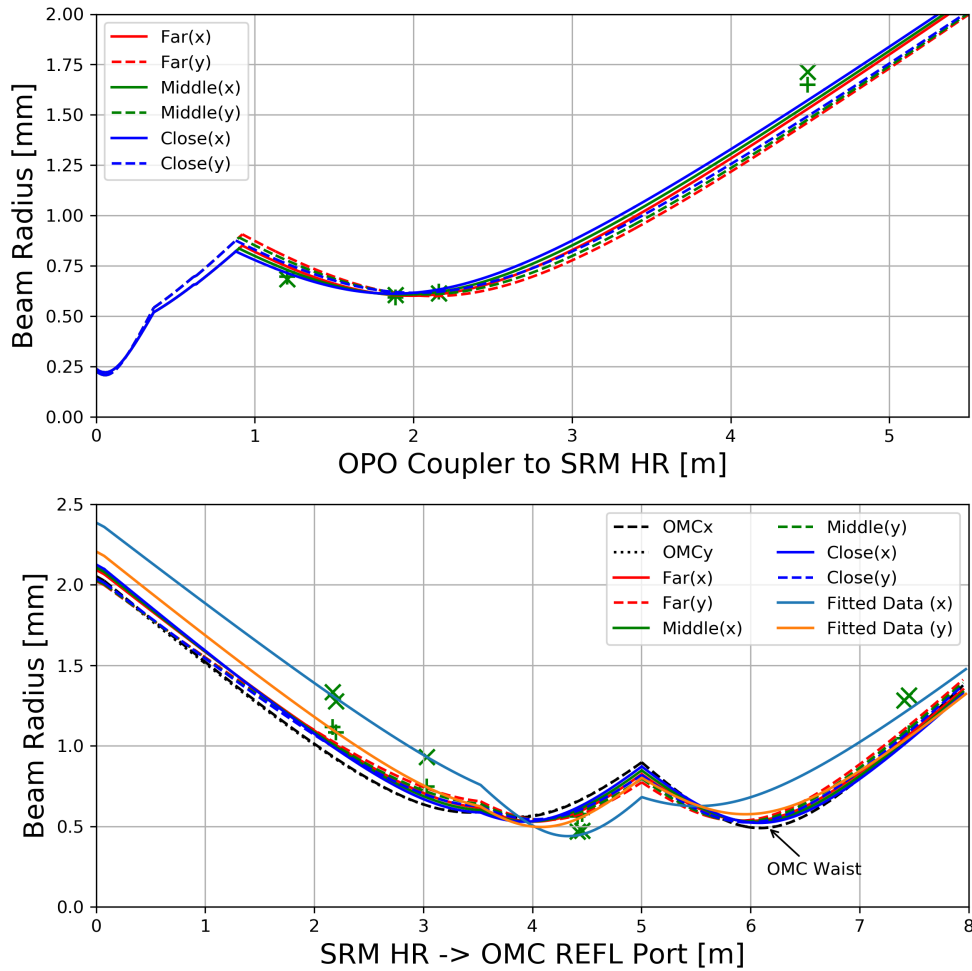


Figure 1.20: **Mode measurement from the OPO.** The results without Lens2 are shown in black for two transverse directions (x/y) and constrain the distance of Lens1 relative to the OPO output. Then, Lens2 is replaced back in its original position on a translation stage at half the range and measurements were taken in order to constrain the distance between Lens1 and Lens2. The beam sizes were fit to find the Gaussian q-parameter entering HAM5. There is some slight deviation in the transverse directions after Lens2, possibly from misalignment of the lens. This method seems to provide a good model of what beam is being injected from the squeezer side.

optics is the largest systematic error especially in the near-field where beam sizes do not change very much as a function of  $\hat{z}$ . In addition, places to put a beam profile become very limited as HAM6 becomes crowded with optical components. In preparation for squeezing in Advanced LIGO, the mode matching from the OPO to OMC was measured and found to be approximately 84% at best. When implementing a telescope with fast lenses, the distances between optics must be stringently characterized but the OPO platform is very crowded along the output path so it was very difficult to accurately measure the path lengths with a ruler. Between the second lens and ZM1, the table is much clearer and by removing Lens2, the Gouy phase is approximately in the far-field which means the distance measurements can be more easily measured as a function of beam size.



**Figure 1.21: Projecting the modes from the squeezer to the OMC.** Determining the actuation range with the translation stage using the as-installed focal lengths,  $f_{\text{Lens}1} = 111$  mm and  $f_{\text{Lens}2} = 334$  mm, showed that the mode matching into the OMC was at most 80% with various translation stage positions with "Close" referring to the position of Lens2 relative to the OPO cavity. Here, crosses represent the transverse-x direction and pluses denote the transverse-y orientation. One very interesting feature is that the astigmatism as measured seems to be worse after re-entering HAM6 from HAM5 and is not explainable by the slight deviations shown in Figure 1.20, so it is possible that some sort of clipping occurs while propagating through the main output Faraday isolator. Near the OMC waist, the predicted mode shapes for different translation stage positions agree with the measured beam sizes and power overlaps were confirmed to be accurate with OMC scans to within a percent.



**Figure 1.22: Repeated measurements made with new lenses.** With the poor mode matching shown in Figure 1.23, the fast telescope lenses needed to be replaced or risk being the limit to effective squeezing for O3. The available range in the translation stage did not allow for increased matching and the crowded OPO platform did not permit coarse moves of Lens1 or Lens2. The next option was replacing the lenses with a solution which did not incorporate large actuation range but was more suited for mode matching. There were a few clean lenses available that provided the right solution but greatly reduced the translation stage efficacy, on the other hand, this made the telescope placement much more robust to path length errors which is the original problem to begin with.

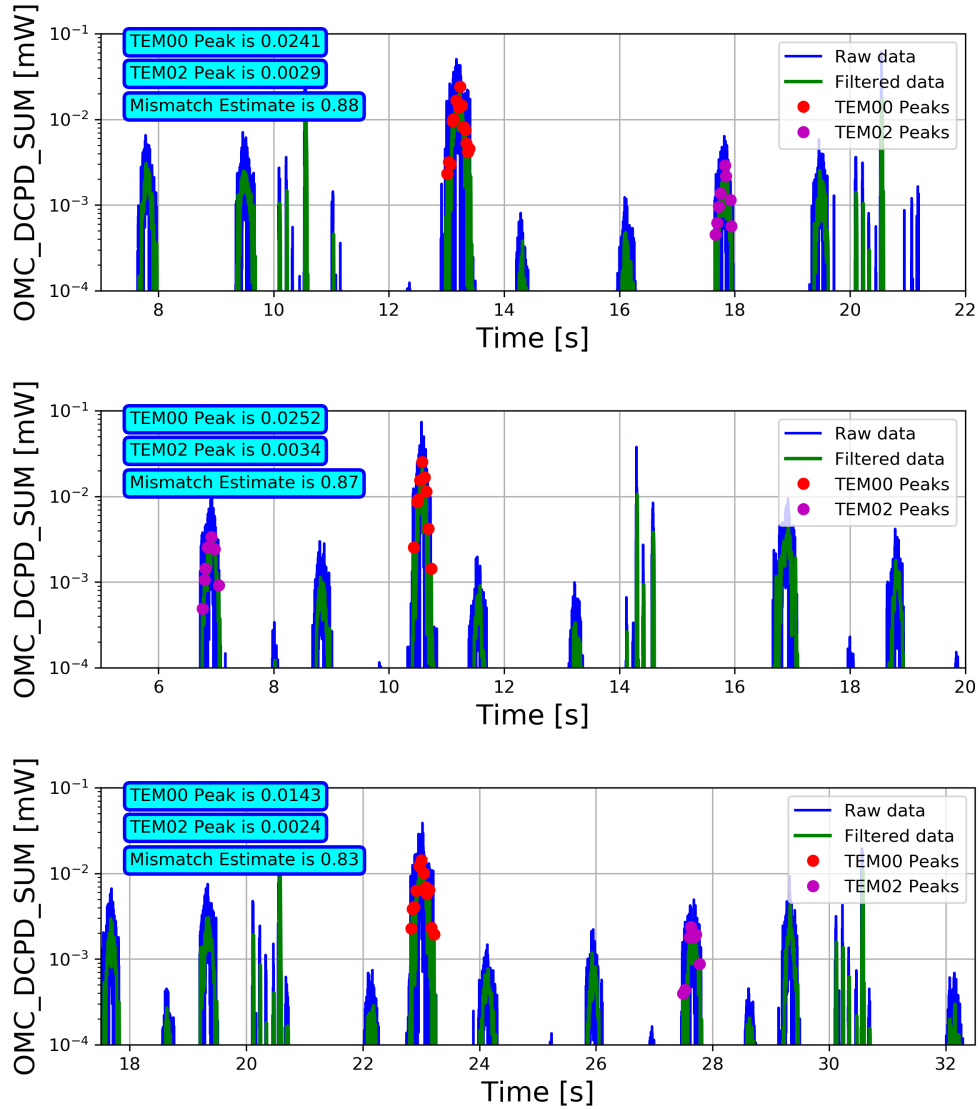


Figure 1.23: **OPO to OMC cavity scanning for various Lens2 positions.** The top figure has the lens closest to the OPO along the propagation axis, the middle figure represents Lens2 at half the actuation range and the bottom figure shows the lens furthest from the OPO. During this time, the OMC ASC control loops were closed on the reflected QPDs to minimize the odd order mode coupling.

# List of Figures

1.1	A simplified model for the effect of a substrate thermal lens on the carrier field.	7
1.2	A plane wave passing through a lens with a temperature gradient. . . . .	10
1.3	A conceptual model of flux balance for a cylindrical object. . . . .	12
1.4	ITM Hartmann sensors optical layout. . . . .	21
1.5	Noise spectra for the HWS spherical lensing. . . . .	22
1.6	ITMX Hartmann Sensor output. . . . .	23
1.7	Clipping on ITMX Hartmann Sensor. . . . .	24
1.8	A time series of the interferometer power increase sequence. . . . .	25
1.9	ITMX gradient plots (left) and wavefront maps (right) during a power up to 30 Watts of input power. . . . .	26
1.10	ITMY gradient plots (left) and wavefront maps (right) during a power up to 30 Watts of input power. . . . .	27
1.11	Thermal lensing as seen by the ITM Hartmann Sensors after a lock loss. .	29
1.12	Posterior distributions from fitting the Hartmann sensor spherical power. .	30
1.13	Calculated TCS settings to balance the substrate lens. . . . .	31
1.14	Mode matching the arm cavities to the power recycling cavity. . . . .	32
1.15	Comparing 3-D plots of the optical path distortion for ITMX and ITMY test masses after powering up the interferometer. . . . .	37
1.16	Interferometer DC powers as a function of round trip arm loss and test mass absorption. . . . .	39

1.17	Model of POP-18 as a function of differential thermal lensing using FINESSE.	40
1.18	Vertex open loop transfer functions while in Nominal Low Noise. . . . .	41
1.19	Measuring vertex optical gains as a function of heating. . . . .	42
1.20	Mode measurement from the OPO. . . . .	43
1.21	Projecting the modes from the squeezer to the OMC. . . . .	45
1.22	Repeated measurements made with new lenses. . . . .	46
1.23	OPO to OMC cavity scanning for various Lens2 positions. . . . .	47

# List of Tables

- 1.1 Single pass actuator lensing calibrations for aLIGO TCS in micro-diopters/Watt. 33

# Bibliography

- [1] J. Abadie et al. Sensitivity Achieved by the LIGO and Virgo Gravitational Wave Detectors during LIGO’s Sixth and Virgo’s Second and Third Science Runs. *arXiv*, 2012.
- [2] B. P. e. a. Abbott. Observation of gravitational waves from a binary black hole merger. *Phys. Rev. Lett.*, 116:061102, Feb 2016. doi: 10.1103/PhysRevLett.116.061102. URL <https://link.aps.org/doi/10.1103/PhysRevLett.116.061102>. 1
- [3] B. P. e. a. Abbott. Gw170817: Observation of gravitational waves from a binary neutron star inspiral. *Phys. Rev. Lett.*, 119:161101, Oct 2017. doi: 10.1103/PhysRevLett.119.161101. URL <https://link.aps.org/doi/10.1103/PhysRevLett.119.161101>. 1
- [4] R. Abbott, R. Adhikari, G. Allen, S. Cowley, E. Daw, D. DeBra, J. Giaime, G. Hammond, M. Hammond, C. Hardham, J. How, W. Hua, W. Johnson, B. Lantz, K. Mason, R. Mittleman, J. Nichol, S. Richman, J. Rollins, D. Shoemaker, G. Stapfer, and R. Stebbins. Seismic isolation for advanced ligo. *Classical and Quantum Gravity*, 19(7):1591, 2002. URL <http://stacks.iop.org/0264-9381/19/i=7/a=349>.
- [5] and and. Ix. a determination of the deflection of light by the sun’s gravitational field, from observations made at the total eclipse of may 29, 1919. *Philosophical Transactions of the Royal Society of London A: Mathematical, Physical and Engineering Sciences*, 220(571-581):291–333, 1920. ISSN 0264-3952. doi: 10.1098/rsta.1920.0009. URL <http://rsta.royalsocietypublishing.org/content/220/571-581/291>.

- [6] D. Z. Anderson. Alignment of resonant optical cavities. *Appl. Opt.*, 23(17):2944–2949, Sep 1984. doi: 10.1364/AO.23.002944. URL <http://ao.osa.org/abstract.cfm?URI=ao-23-17-2944>.
- [7] M. Beijersbergen, L. Allen, H. van der Veen, and J. Woerdman. Astigmatic laser mode converters and transfer of orbital angular momentum. *Optics Communications*, 96(1):123 – 132, 1993. ISSN 0030-4018. doi: [https://doi.org/10.1016/0030-4018\(93\)90535-D](https://doi.org/10.1016/0030-4018(93)90535-D). URL <http://www.sciencedirect.com/science/article/pii/003040189390535D>.
- [8] P. G. Bergmann. Summary of the chapel hill conference. *Rev. Mod. Phys.*, 29:352–354, Jul 1957. doi: 10.1103/RevModPhys.29.352. URL <https://link.aps.org/doi/10.1103/RevModPhys.29.352>.
- [9] E. D. Black. An introduction to pound–drever–hall laser frequency stabilization. *American Journal of Physics*, 69(1):79–87, 2001. doi: 10.1119/1.1286663. URL <https://doi.org/10.1119/1.1286663>.
- [10] D. G. Blair. *The detection of gravitational waves*. Cambridge University Press, 2005.
- [11] C. Bond, D. Brown, A. Freise, and K. A. Strain. Interferometer techniques for gravitational-wave detection. *Living Reviews in Relativity*, 19(1):3, Feb 2017. ISSN 1433-8351. doi: 10.1007/s41114-016-0002-8. URL <https://doi.org/10.1007/s41114-016-0002-8>.
- [12] C. e. a. Bond. Finesse input files for the h1 interferometer. URL <https://dcc.ligo.org/LIGO-T1300904>.
- [13] A. Brooks, P. Veitch, J. Munch, and T.-L. Kelly. An off-axis hartmann sensor for the measurement of absorption-induced wavefront distortion in advanced gravitational wave interferometers. *General Relativity and Gravitation*, 37(9):1575–1580, Sep 2005. ISSN 1572-9532. doi: 10.1007/s10714-005-0137-5. URL <https://doi.org/10.1007/s10714-005-0137-5>. 19

- [14] A. F. Brooks. *Hartmann Wavefront Sensors for Advanced Gravitational Wave*. PhD thesis, The University of Adelaide, 7 2007. 20
- [15] A. F. Brooks, T.-L. Kelly, P. J. Veitch, and J. Munch. Ultra-sensitive wavefront measurement using a hartmann sensor. *Opt. Express*, 15(16):10370–10375, Aug 2007. doi: 10.1364/OE.15.010370. URL <http://www.opticsexpress.org/abstract.cfm?URI=oe-15-16-10370>. 19
- [16] A. F. Brooks, D. Hosken, J. Munch, P. J. Veitch, Z. Yan, C. Zhao, Y. Fan, L. Ju, D. Blair, P. Willems, B. Slagmolen, and J. Degallaix. Direct measurement of absorption-induced wavefront distortion in high optical power systems. *Appl. Opt.*, 48(2):355–364, Jan 2009. doi: 10.1364/AO.48.000355. URL <http://ao.osa.org/abstract.cfm?URI=ao-48-2-355>. 19
- [17] A. F. Brooks, B. Abbott, M. A. Arain, G. Ciani, A. Cole, G. Grabeel, E. Gustafson, C. Guido, M. Heintze, A. Heptonstall, M. Jacobson, W. Kim, E. King, A. Lynch, S. O’Connor, D. Ottaway, K. Mailand, G. Mueller, J. Munch, V. Sannibale, Z. Shao, M. Smith, P. Veitch, T. Vo, C. Vorvick, and P. Willems. Overview of advanced ligo adaptive optics. *Appl. Opt.*, 55(29):8256–8265, Oct 2016. doi: 10.1364/AO.55.008256. URL <http://ao.osa.org/abstract.cfm?URI=ao-55-29-8256>. 18, 20, 21, 22
- [18] D. Brown. Personal Communication, 2018. 28
- [19] A. Buonanno and Y. Chen. Quantum noise in second generation, signal-recycled laser interferometric gravitational-wave detectors. *Phys. Rev. D*, 64:042006, Jul 2001. doi: 10.1103/PhysRevD.64.042006. URL <https://link.aps.org/doi/10.1103/PhysRevD.64.042006>.
- [20] S. M. Carroll. *Spacetime and geometry: an introduction to general relativity*. Pearson, 2003.

- [21] C. M. Caves. Quantum-mechanical noise in an interferometer. *Phys. Rev. D*, 23:1693–1708, Apr 1981. doi: 10.1103/PhysRevD.23.1693. URL <https://link.aps.org/doi/10.1103/PhysRevD.23.1693>.
- [22] C. M. Caves and B. L. Schumaker. New formalism for two-photon quantum optics. i. quadrature phases and squeezed states. *Phys. Rev. A*, 31:3068–3092, May 1985. doi: 10.1103/PhysRevA.31.3068. URL <https://link.aps.org/doi/10.1103/PhysRevA.31.3068>.
- [23] C. M. Caves, K. S. Thorne, R. W. P. Drever, V. D. Sandberg, and M. Zimmermann. On the measurement of a weak classical force coupled to a quantum-mechanical oscillator. i. issues of principle. *Rev. Mod. Phys.*, 52:341–392, Apr 1980. doi: 10.1103/RevModPhys.52.341. URL <https://link.aps.org/doi/10.1103/RevModPhys.52.341>.
- [24] J. L. Cervantes-Cota, S. Galindo-Uribarri, and G. F. Smoot. A brief history of gravitational waves. *Universe*, 2(3), 2016. ISSN 2218-1997. doi: 10.3390/universe2030022. URL <http://www.mdpi.com/2218-1997/2/3/22>.
- [25] Y. Chen, S. L. Danilishin, F. Y. Khalili, and H. Müller-Ebhardt. Qnd measurements for future gravitational-wave detectors. *General Relativity and Gravitation*, 43(2):671–694, Feb 2011. ISSN 1572-9532. doi: 10.1007/s10714-010-1060-y. URL <https://doi.org/10.1007/s10714-010-1060-y>.
- [26] S. S. Y. Chua. *Quantum Enhancement of a 4km Laser Interferometer Gravitational-Wave Detector*. PhD thesis, The Australian National University, 4 2013.
- [27] L. Collaboration. Ligo optics. URL <https://galaxy.ligo.caltech.edu/optics/>.
- [28] T. L. S. Collaboration. A gravitational wave observatory operating beyond the quantum shot-noise limit. *Nature Physics*, 7:962, Nov 2009. doi: 10.1038/nphys2083. URL <http://dx.doi.org/10.1038/nphys2083>.

- [29] T. L. S. Collaboration. Enhanced sensitivity of the ligo gravitational wave detector by using squeezed states of light. *Nature Physics*, 7:613, Jul 2013. doi: 10.1038/nphoton.2013.177. URL <http://dx.doi.org/10.1038/nphoton.2013.177>.
- [30] T. L. S. Collaboration. Advanced ligo. *Classical and Quantum Gravity*, 32(7):074001, 2015. URL <http://stacks.iop.org/0264-9381/32/i=7/a=074001>.
- [31] H. Collins. *Gravity's shadow: the search for gravitational waves*. University of Chicago Press, 2004.
- [32] R. DeRosa, J. C. Driggers, D. Atkinson, H. Miao, V. Frolov, M. Landry, J. A. Giaime, and R. X. Adhikari. Global feed-forward vibration isolation in a km scale interferometer. *Classical and Quantum Gravity*, 29(21):215008, 2012. URL <http://stacks.iop.org/0264-9381/29/i=21/a=215008>.
- [33] J. C. Driggers, J. Harms, and R. X. Adhikari. Subtraction of newtonian noise using optimized sensor arrays. , 86(10):102001, Nov. 2012. doi: 10.1103/PhysRevD.86.102001.
- [34] S. Dwyer, L. Barsotti, S. S. Y. Chua, M. Evans, M. Factourovich, D. Gustafson, T. Isogai, K. Kawabe, A. Khalaidovski, P. K. Lam, M. Landry, N. Mavalvala, D. E. McClelland, G. D. Meadors, C. M. Mow-Lowry, R. Schnabel, R. M. S. Schofield, N. Smith-Lefebvre, M. Stefszky, C. Vorvick, and D. Sigg. Squeezed quadrature fluctuations in a gravitational wave detector using squeezed light. *Opt. Express*, 21(16):19047–19060, Aug 2013. doi: 10.1364/OE.21.019047. URL <http://www.opticsexpress.org/abstract.cfm?URI=oe-21-16-19047>.
- [35] A. Einstein. Die grundlage der allgemeinen relativitätstheorie. *Annalen der Physik*, 354(7):769–822, 1905. doi: 10.1002/andp.19163540702. URL <https://onlinelibrary.wiley.com/doi/abs/10.1002/andp.19163540702>.
- [36] A. Einstein. Investigations on the theory of the brownian movement. *Ann. der*

- Physik*, 1905. URL [http://www.physik.fu-berlin.de/~{}kleinert/files/eins\\_brownian.pdf](http://www.physik.fu-berlin.de/~{}kleinert/files/eins_brownian.pdf).
- [37] A. Einstein. Zur Elektrodynamik bewegter Körper. (German) [On the electrodynamics of moving bodies]. *Annalen der Physik*, 322(10):891–921, 1905. doi: <http://dx.doi.org/10.1002/andp.19053221004>.
- [38] R. W. et al. Ligo document m890001-v3, 1989. URL <https://dcc.ligo.org/LIGO-M890001/public>.
- [39] M. Evans, S. Ballmer, M. Fejer, P. Fritschel, G. Harry, and G. Ogin. Thermo-optic noise in coated mirrors for high-precision optical measurements. *Phys. Rev. D*, 78:102003, Nov 2008. doi: [10.1103/PhysRevD.78.102003](https://doi.org/10.1103/PhysRevD.78.102003). URL <https://link.aps.org/doi/10.1103/PhysRevD.78.102003>.
- [40] M. Evans, L. Barsotti, P. Kwee, J. Harms, and H. Miao. Realistic filter cavities for advanced gravitational wave detectors. *Phys. Rev. D*, 88:022002, Jul 2013. doi: [10.1103/PhysRevD.88.022002](https://doi.org/10.1103/PhysRevD.88.022002). URL <https://link.aps.org/doi/10.1103/PhysRevD.88.022002>.
- [41] L. S. Finn. Binary inspiral, gravitational radiation, and cosmology. *Phys. Rev.*, D53: 2878–2894, 1996. doi: [10.1103/PhysRevD.53.2878](https://doi.org/10.1103/PhysRevD.53.2878).
- [42] D. Foreman-Mackey, D. W. Hogg, D. Lang, and J. Goodman. emcee : The mcmc hammer. *Publications of the Astronomical Society of the Pacific*, 125(925):306, 2013. URL <http://stacks.iop.org/1538-3873/125/i=925/a=306>. 30
- [43] P. Fritschel, D. Shoemaker, and R. Weiss. Demonstration of light recycling in a michelson interferometer with fabry–perot cavities. *Appl. Opt.*, 31(10):1412–1418, Apr 1992. doi: [10.1364/AO.31.001412](https://doi.org/10.1364/AO.31.001412). URL <http://ao.osa.org/abstract.cfm?URI=ao-31-10-1412>.

- [44] P. Fritschel, N. Mavalvala, D. Shoemaker, D. Sigg, M. Zucker, and G. González. Alignment of an interferometric gravitational wave detector. *Appl. Opt.*, 37(28):6734–6747, Oct 1998. doi: 10.1364/AO.37.006734. URL <http://ao.osa.org/abstract.cfm?URI=ao-37-28-6734>.
- [45] P. Fritschel, R. Bork, G. González, N. Mavalvala, D. Ouimette, H. Rong, D. Sigg, and M. Zucker. Readout and control of a power-recycled interferometric gravitational-wave antenna. *Appl. Opt.*, 40(28):4988–4998, Oct 2001. doi: 10.1364/AO.40.004988. URL <http://ao.osa.org/abstract.cfm?URI=ao-40-28-4988>.
- [46] P. Fritschel, R. Bork, G. González, N. Mavalvala, D. Ouimette, H. Rong, D. Sigg, and M. Zucker. Readout and control of a power-recycled interferometric gravitational-wave antenna. *Appl. Opt.*, 40(28):4988–4998, Oct 2001. doi: 10.1364/AO.40.004988. URL <http://ao.osa.org/abstract.cfm?URI=ao-40-28-4988>.
- [47] C. C. Gerry and P. Knight. *Introductory quantum optics*. Cambridge University Press, 2005.
- [48] G. I. González and P. R. Saulson. Brownian motion of a mass suspended by an anelastic wire. *The Journal of the Acoustical Society of America*, 96(1):207–212, 1994. doi: 10.1121/1.410467. URL <https://doi.org/10.1121/1.410467>.
- [49] D. J. Griffiths. *Introduction to quantum mechanics*. Pearson Prentice Hall, 2005.
- [50] G. M. Harry, A. M. Gretarsson, P. R. Saulson, S. E. Kittelberger, S. D. Penn, W. J. Startin, S. Rowan, M. M. Fejer, D. R. M. Crooks, G. Cagnoli, J. Hough, and N. Nakagawa. Thermal noise in interferometric gravitational wave detectors due to dielectric optical coatings. *Classical and Quantum Gravity*, 19(5):897, 2002. URL <http://stacks.iop.org/0264-9381/19/i=5/a=305>.
- [51] Y. Hefetz, N. Mavalvala, and D. Sigg. Principles of calculating alignment signals in complex resonant optical interferometers. *J. Opt. Soc. Am. B*, 14(7):1597–1606, Jul

1997. doi: 10.1364/JOSAB.14.001597. URL <http://josab.osa.org/abstract.cfm?URI=josab-14-7-1597>.
- [52] P. Hello and J.-Y. Vinet. Analytical models of thermal aberrations in massive mirrors heated by high power laser beams. *Journal de Physique*, 51(12):1267–1282, 1990. doi: 10.1051/jphys:0199000510120126700. 10
- [53] S. Hild, H. Grote, J. Degallaix, S. Chelkowski, K. Danzmann, A. Freise, M. Hewitson, J. Hough, H. Lück, M. Prijatelj, K. A. Strain, J. R. Smith, and B. Willke. Dc-readout of a signal-recycled gravitational wave detector. *Classical and Quantum Gravity*, 26(5):055012, 2009. URL <http://stacks.iop.org/0264-9381/26/i=5/a=055012>.
- [54] S. A. Hughes and K. S. Thorne. Seismic gravity-gradient noise in interferometric gravitational-wave detectors. *Phys. Rev. D*, 58:122002, Nov 1998. doi: 10.1103/PhysRevD.58.122002. URL <https://link.aps.org/doi/10.1103/PhysRevD.58.122002>.
- [55] I. K. and S. D. Frequency response of the aligo interferometer: part1. Technical report, California Institute of Technology, 2015. URL <https://dcc.ligo.org/LIGO-T1500325>.
- [56] I. K., S. D., and K. K. Frequency response of the aligo interferometer: part2. Technical report, California Institute of Technology, 2015. URL <https://dcc.ligo.org/LIGO-T1500461>.
- [57] I. K., S. D., and K. K. Frequency response of the aligo interferometer: part3. Technical report, California Institute of Technology, 2015. URL <https://dcc.ligo.org/LIGO-T1500559>.
- [58] H. J. Kimble, Y. Levin, A. B. Matsko, K. S. Thorne, and S. P. Vyatchanin. Conversion of conventional gravitational-wave interferometers into quantum nondemolition interferometers by modifying their input and/or output optics. *Phys. Rev. D*, 65:022002,

- Dec 2001. doi: 10.1103/PhysRevD.65.022002. URL <https://link.aps.org/doi/10.1103/PhysRevD.65.022002>.
- [59] H. Kogelnik and T. Li. Laser beams and resonators. *Appl. Opt.*, 5(10):1550–1567, Oct 1966. doi: 10.1364/AO.5.001550. URL <http://ao.osa.org/abstract.cfm?URI=ao-5-10-1550>.
- [60] R. Lawrence, M. Zucker, P. Fritschel, P. Marfuta, and D. Shoemaker. Adaptive thermal compensation of test masses in advanced ligo. *Classical and Quantum Gravity*, 19(7):1803, 2002. URL <http://stacks.iop.org/0264-9381/19/i=7/a=377>. 6, 9, 18
- [61] O. D. M Rakhmanov, F Bondu and R. L. S. Jr. Characterization of the ligo 4 km fabry–perot cavities via their high-frequency dynamic responses to length and laser frequency variations. *Classical and Quantum Gravity*, Feb 2004. URL <http://iopscience.iop.org/article/10.1088/0264-9381/21/5/015/meta>.
- [62] F. Magana-Sandoval. Adaptive mode matching upgrade for advanced ligo. URL <https://dcc.ligo.org/LIGO-P1800143>.
- [63] F. Maticichard, B. Lantz, K. Mason, R. Mittleman, B. Abbott, S. Abbott, E. Allwine, S. Barnum, J. Birch, S. Biscans, D. Clark, D. Coyne, D. DeBra, R. DeRosa, S. Foley, P. Fritschel, J. Giaime, C. Gray, G. Grabeel, J. Hanson, M. Hillard, J. Kissel, C. Kucharczyk, A. L. Roux, V. Lhuillier, M. Macinnis, B. O'Reilly, D. Ottaway, H. Paris, M. Puma, H. Radkins, C. Ramet, M. Robinson, L. Ruet, P. Sareen, D. Shoemaker, A. Stein, J. Thomas, M. Vargas, and J. Warner. Advanced ligo two-stage twelve-axis vibration isolation and positioning platform. part 1: Design and production overview. *Precision Engineering*, 40:273 – 286, 2015. ISSN 0141-6359. doi: <https://doi.org/10.1016/j.precisioneng.2014.09.010>. URL <http://www.sciencedirect.com/science/article/pii/S0141635914001561>.
- [64] F. Maticichard, B. Lantz, K. Mason, R. Mittleman, B. Abbott, S. Abbott, E. All-

- wine, S. Barnum, J. Birch, S. Biscans, D. Clark, D. Coyne, D. DeBra, R. DeRosa, S. Foley, P. Fritschel, J. Giaime, C. Gray, G. Grabeel, J. Hanson, M. Hillard, J. Kissel, C. Kucharczyk, A. L. Roux, V. Lhuillier, M. Macinnis, B. O'Reilly, D. Ottaway, H. Paris, M. Puma, H. Radkins, C. Ramet, M. Robinson, L. Ruet, P. Sarreen, D. Shoemaker, A. Stein, J. Thomas, M. Vargas, and J. Warner. Advanced ligo two-stage twelve-axis vibration isolation and positioning platform. part 2: Experimental investigation and tests results. *Precision Engineering*, 40:287 – 297, 2015. ISSN 0141-6359. doi: <https://doi.org/10.1016/j.precisioneng.2014.11.010>. URL <http://www.sciencedirect.com/science/article/pii/S0141635914002098>.
- [65] F. Matichard, B. Lantz, R. Mittleman, K. Mason, J. Kissel, B. Abbott, S. Biscans, J. McIver, R. Abbott, S. Abbott, E. Allwine, S. Barnum, J. Birch, C. Celerier, D. Clark, D. Coyne, D. DeBra, R. DeRosa, M. Evans, S. Foley, P. Fritschel, J. A. Giaime, C. Gray, G. Grabeel, J. Hanson, C. Hardham, M. Hillard, W. Hua, C. Kucharczyk, M. Landry, A. L. Roux, V. Lhuillier, D. Macleod, M. Macinnis, R. Mitchell, B. O'Reilly, D. Ottaway, H. Paris, A. Pele, M. Puma, H. Radkins, C. Ramet, M. Robinson, L. Ruet, P. Sarin, D. Shoemaker, A. Stein, J. Thomas, M. Vargas, K. Venkateswara, J. Warner, and S. Wen. Seismic isolation of advanced ligo: Review of strategy, instrumentation and performance. *Classical and Quantum Gravity*, 32(18):185003, 2015. URL <http://stacks.iop.org/0264-9381/32/i=18/a=185003>.
- [66] E. Morrison, B. J. Meers, D. I. Robertson, and H. Ward. Automatic alignment of optical interferometers. *Appl. Opt.*, 33(22):5041–5049, Aug 1994. doi: 10.1364/AO.33.005041. URL <http://ao.osa.org/abstract.cfm?URI=ao-33-22-5041>.
- [67] G. Mueller, Q. ze Shu, R. Adhikari, D. B. Tanner, D. Reitze, D. Sigg, N. Mavalvala, and J. Camp. Determination and optimization of mode matching into optical cavities by heterodyne detection. *Opt. Lett.*, 25(4):266–268, Feb 2000. doi: 10.1364/OL.25.000266. URL <http://ol.osa.org/abstract.cfm?URI=ol-25-4-266>.

- [68] E. Oelker, T. Isogai, J. Miller, M. Tse, L. Barsotti, N. Mavalvala, and M. Evans. Audio-band frequency-dependent squeezing for gravitational-wave detectors. *Phys. Rev. Lett.*, 116:041102, Jan 2016. doi: 10.1103/PhysRevLett.116.041102. URL <https://link.aps.org/doi/10.1103/PhysRevLett.116.041102>.
- [69] U. of Birmingham. *Finesse Manual*, 2014. URL <http://www.gwoptics.org/finesse/>.
- [70] A. T. O’Neil and J. Courtial. Mode transformations in terms of the constituent hermite–gaussian or laguerre–gaussian modes and the variable-phase mode converter. *Optics Communications*, 181(1):35 – 45, 2000. ISSN 0030-4018. doi: [https://doi.org/10.1016/S0030-4018\(00\)00736-7](https://doi.org/10.1016/S0030-4018(00)00736-7). URL <http://www.sciencedirect.com/science/article/pii/S0030401800007367>.
- [71] A. Perreca, J. Lough, D. Kelley, and S. W. Ballmer. Multidimensional optical trapping of a mirror. *Phys. Rev. D*, 89:122002, Jun 2014. doi: 10.1103/PhysRevD.89.122002. URL <https://link.aps.org/doi/10.1103/PhysRevD.89.122002>.
- [72] F. A. E. Pirani. Republication of: On the physical significance of the riemann tensor. *General Relativity and Gravitation*, 41(5):1215–1232, May 2009. ISSN 1572-9532. doi: 10.1007/s10714-009-0787-9. URL <https://doi.org/10.1007/s10714-009-0787-9>.
- [73] J. Ramette, M. Kasprzack, A. Brooks, C. Blair, H. Wang, and M. Heintze. Analytical model for ring heater thermal compensation in the advanced laser interferometer gravitational-wave observatory. *Appl. Opt.*, 55(10):2619–2625, Apr 2016. doi: 10.1364/AO.55.002619. URL <http://ao.osa.org/abstract.cfm?URI=ao-55-10-2619>. 28
- [74] B. E. A. Saleh and M. C. Teich. *Fundamentals of Photonics*. Wiley-Interscience, 2009.
- [75] P. Saulson. *Fundamentals of Gravitational Wave Detectors*. World Scientific, 2016.
- [76] P. R. Saulson. Terrestrial gravitational noise on a gravitational wave antenna. *Phys.*

- Rev. D*, 30:732–736, Aug 1984. doi: 10.1103/PhysRevD.30.732. URL <https://link.aps.org/doi/10.1103/PhysRevD.30.732>.
- [77] P. R. Saulson. Thermal noise in mechanical experiments. *Phys. Rev. D*, 42:2437–2445, Oct 1990. doi: 10.1103/PhysRevD.42.2437. URL <https://link.aps.org/doi/10.1103/PhysRevD.42.2437>.
- [78] P. R. Saulson. If light waves are stretched by gravitational waves, how can we use light as a ruler to detect gravitational waves? *American Journal of Physics*, 65(6):501–505, 1997. doi: 10.1119/1.18578. URL <https://doi.org/10.1119/1.18578>.
- [79] B. Schutz. *A First Course in General Relativity*. Cambridge University Press, 2009.
- [80] B. F. Schutz. *A first course in general relativity*. Cambridge University Press, 2009.
- [81] R. Shankar. *Principles of Quantum Mechanics*. Springer Verlag, 2014.
- [82] J. A. Sidles and D. Sigg. Optical torques in suspended fabry–perot interferometers. *Physics Letters A*, 354(3):167 – 172, 2006. ISSN 0375-9601. doi: <https://doi.org/10.1016/j.physleta.2006.01.051>. URL <http://www.sciencedirect.com/science/article/pii/S0375960106001381>.
- [83] K. Strain, K. Danzmann, J. Mizuno, P. Nelson, A. Rüdiger, R. Schilling, and W. Winkler. Thermal lensing in recycling interferometric gravitational wave detectors. *Physics Letters A*, 194(1):124 – 132, 1994. ISSN 0375-9601. doi: [https://doi.org/10.1016/0375-9601\(94\)00717-4](https://doi.org/10.1016/0375-9601(94)00717-4). URL <http://www.sciencedirect.com/science/article/pii/0375960194007174>. 18
- [84] P. Veitch, A. Brooks, W. Kim, C. Blair, H. Cao, G. Grabeel, T. Hardwick, M. Heintze, A. Heponstall, C. Ingram, J. Munch, D. Ottaway, and T. Vo. Hartmann wavefront sensors for advanced ligo. In *Conference on Lasers and Electro-Optics*, page SW3M.5.

- Optical Society of America, 2018. doi: 10.1364/CLEO\_SI.2018.SW3M.5. URL [http://www.osapublishing.org/abstract.cfm?URI=CLEO\\_SI-2018-SW3M.5](http://www.osapublishing.org/abstract.cfm?URI=CLEO_SI-2018-SW3M.5). 19
- [85] J.-Y. Vinet. On special optical modes and thermal issues in advanced gravitational wave interferometric detectors. *Living Reviews in Relativity*, 12(1):5, Jul 2009. ISSN 1433-8351. doi: 10.12942/lrr-2009-5. URL <https://doi.org/10.12942/lrr-2009-5>. 10, 15, 34
- [86] H. Wang, C. Blair, M. D. Álvarez, A. Brooks, M. F. Kasprzack, J. Ramette, P. M. Meyers, S. Kaufer, B. O'Reilly, C. M. Mow-Lowry, and A. Freise. Thermal modelling of advanced ligo test masses. *Classical and Quantum Gravity*, 34(11):115001, 2017. URL <http://stacks.iop.org/0264-9381/34/i=11/a=115001>. 28
- [87] J. Weber. Evidence for discovery of gravitational radiation. *Phys. Rev. Lett.*, 22:1320–1324, Jun 1969. doi: 10.1103/PhysRevLett.22.1320. URL <https://link.aps.org/doi/10.1103/PhysRevLett.22.1320>.
- [88] J. M. Weisberg, J. H. Taylor, and L. A. Fowler. Gravitational waves from an orbiting pulsar. *Scientific American*, 245(4):74–83, 1981. ISSN 00368733, 19467087. URL <http://www.jstor.org/stable/24964580>.
- [89] W. Winkler, K. Danzmann, A. Rüdiger, and R. Schilling. Heating by optical absorption and the performance of interferometric gravitational-wave detectors. *Phys. Rev. A*, 44:7022–7036, Dec 1991. doi: 10.1103/PhysRevA.44.7022. URL <https://link.aps.org/doi/10.1103/PhysRevA.44.7022>. 6, 18
- [90] H. Yu, D. Martynov, S. Vitale, M. Evans, D. Shoemaker, B. Barr, G. Hammond, S. Hild, J. Hough, S. Huttner, S. Rowan, B. Sorazu, L. Carbone, A. Freise, C. Mow-Lowry, K. L. Dooley, P. Fulda, H. Grote, and D. Sigg. Prospects for detecting gravitational waves at 5 hz with ground-based detectors. *Phys. Rev. Lett.*, 120:141102, Apr 2018.

doi: 10.1103/PhysRevLett.120.141102. URL <https://link.aps.org/doi/10.1103/PhysRevLett.120.141102>.